SPECIAL
DYNAMO/CINDY/AMIE/LASP
COLLECTION

Sounding-Based Thermodynamic Budgets for DYNAMO

RICHARD H. JOHNSON, PAUL E. CIESIELSKI, AND JAMES H. RUPPERT JR.

Colorado State University, Fort Collins, Colorado

MASAKI KATSUMATA

Japan Agency for Marine-Earth Science and Technology, Yokosuka, Japan

ABSTRACT

The Dynamics of the Madden–Julian Oscillation (DYNAMO) field campaign, conducted over the Indian Ocean from October 2011 to March 2012, was designed to study the initiation of the Madden–Julian oscillation (MJO). Two prominent MJOs occurred in the experimental domain during the special observing period in October and November. Data from a northern and a southern sounding array (NSA and SSA, respectively) have been used to investigate the apparent heat sources and sinks (Q_1 and Q_2) and radiative heating rates Q_R throughout the life cycles of the two MJO events. The MJO signal was far stronger in the NSA than the SSA. Time series of Q_1, Q_2, and the vertical eddy flux of moist static energy reveal an evolution of cloud systems for both MJOs consistent with prior studies: shallow, nonprecipitating cumulus during the suppressed phase, followed by cumulus congestus, then deep convection during the active phase, and finally stratiform precipitation. However, the duration of these phases was shorter for the November MJO than for the October event. The profiles of Q_1 and Q_2 for the two arrays indicate a greater stratiform rain fraction for the NSA than the SSA—a finding supported by TRMM measurements. Surface rainfall rates and net tropospheric Q_R determined as residuals from the budgets show good agreement with satellite-based estimates. The cloud radiative forcing was approximately 20% of the column-integrated convective heating and of the same amplitude as the normalized gross moist stability, leaving open the possibility of radiative–convective instability for the two MJOs.

1. Introduction

The Madden–Julian oscillation (MJO; Madden and Julian 1972) is one of the most prominent features of the general circulation, having global impacts on weather and climate (Zhang 2013). Despite the considerable attention given to the MJO in recent years, there remain significant gaps in understanding and prediction of the phenomenon (Hung et al. 2013; Zhang et al. 2013). A field campaign was conducted over the Indian Ocean from October 2011 to March 2012 to investigate a number of the outstanding issues related to the MJO, with particular attention to tropospheric moistening processes, evolving cloud populations, and air–sea interaction during its initiation. The experiment consisted of four collaborating campaign components (Yoneyama et al. 2013): Dynamics of the MJO (DYNAMO), Cooperative Indian Ocean Experiment on Intraseasonal Variability in the Year 2011 (CINDY), Atmospheric Radiation Measurement Program (ARM) MJO Investigation Experiment (AMIE), and Littoral Air–Sea Processes (LASP). We will refer to the combined effort as DYNAMO.

Emerging from MJO studies over the past several decades is the concept of a distinct, repeatable evolution of precipitation systems within the MJO convective envelope. Namely, cloud populations through the MJO life cycle have been observed where the dominant mode of convection transitions from shallow cumulus to cumulus congestus to deep convection to stratiform precipitation systems (Johnson et al. 1999; Kikuchi and Takayabu 2004; Benedict and Randall 2007; Haertel et al. 2008; Del Genio et al. 2012; Xu and Rutledge 2014). This pattern of evolution is found to occur over a wide range of time and space

Corresponding author address: Richard H. Johnson, Department of Atmospheric Science, 1371 Campus Delivery, Colorado State University, Fort Collins, CO 80523.
E-mail: johnson@atmos.colostate.edu

scales and associated with a variety of tropical disturbances, ranging from individual convective systems to the MJO itself (Kiladis et al. 2005, 2009). Within the framework of the MJO, the pattern is characterized by changing frequency distributions of cloud types through the overall life cycle rather than one cloud type existing in each MJO phase, supportive of the "building block" hypothesis proposed by Mapes et al. (2006). Moreover, there is evidence from the studies of Kikuchi and Takayabu (2004), Yoneyama et al. (2008), Virts and Wallace (2010), Del Genio et al. (2012), and Johnson and Ciesielski (2013) to indicate that the progression of the cloud population in the buildup phase of the MJO actually occurs in a stepwise fashion, with distinct periods of ~1 week or more when there is a dominance of each (cumulus, congestus, cumulonimbus) cloud type. However, the mechanisms by which the atmosphere is moistened during the initiation phase of the MJO are still not well understood and remain a matter of considerable debate (e.g., Waite and Khouider 2010; Hohenegger and Stevens 2013; Barnes and Houze 2013; Powell and Houze 2013; Yuan and Houze 2013).

DYNAMO was designed to explore moistening processes and cloud populations within the MJO using multiple instrument platforms: cloud and precipitation radars, profilers, sounding networks, aircraft, and satellites. This study focuses primarily on one aspect of the DYNAMO measurement system—the sounding network—to compute heat and moisture budgets following the procedures of Yanai et al. (1973), with the goal of inferring properties of convective systems and their roles of latent heating and moistening/drying within the MJO. While there have been numerous studies investigating diabatic heating in the MJO using reanalysis data [for a review, see Zhang et al. (2013)], model-independent computations of MJO heating profiles from field campaigns are limited.

The first opportunity to directly compute heating profiles and moistening processes within the MJO using a network of soundings was for the 1992/93 Tropical Ocean and Global Atmosphere Coupled Atmosphere–Ocean Response Experiment (TOGA COARE; Webster and Lukas 1992). These studies revealed a population of cloud systems within the MJO, progressing from shallow cumulus to congestus to deep convection to stratiform through the life cycle (Lin and Johnson 1996; Johnson and Lin 1997; Johnson et al. 1999; Tung et al. 1999). Diabatic heating profiles were also determined for the 2006 *Mirai* Indian Ocean Cruise for the Study of the MJO Onset (MISMO; Yoneyama et al. 2008). Katsumata et al. (2011) found profiles of apparent heat source Q_1 and apparent moisture sink Q_2 during MISMO for an abortive MJO similar to those for TOGA COARE.

DYNAMO affords a third opportunity to investigate heating and moistening within the MJO, but this time

with improved sounding instrumentation compared to TOGA COARE (Ciesielski et al. 2014a) and with higher time-resolution launches (most sites in the core DYNAMO domain had 3-hourly soundings as opposed to 6-hourly in TOGA COARE). In this study, we compute the apparent heat source Q_1 and apparent moisture sink Q_2 of Yanai et al. (1973) for the DYNAMO sounding arrays and combine the results with independent estimates of surface fluxes to compute surface precipitation and net tropospheric radiative heating rates for the months of October and November 2011. Two prominent MJO events occurred during this period (Gottschalck et al. 2013; Yoneyama et al. 2013; Johnson and Ciesielski 2013). The findings are then compared to satellite-based estimates of those quantities. The DYNAMO sounding array analyses have already formed the basis for large-scale forcing fields being used by various authors, so evaluation of the accuracy of those analyses through comparison with independent estimates is important. The analysis products developed in this study have been recently used by Sobel et al. (2014) to investigate the moist static energy budget for the DYNAMO MJOs.

Observations collected on Gan Island during AMIE have enabled the computation of the vertical profile of radiative heating in the troposphere at that location as a function of time throughout the experiment (Feng et al. 2014). We use these estimates of the radiative heating profile to determine time series of the vertical flux of moist static energy, which provides a measure of cumulus activity (Yanai et al. 1973). This information, along with the fields of Q_1 and Q_2, will be used to infer characteristics of the evolving cloud populations during the DYNAMO MJOs. In addition, the possible role of radiative–convective instability in the MJO (Yu et al. 1998; Raymond 2001; Stephens et al. 2004; Lin and Mapes 2004; Jiang et al. 2011) will be explored based on computations of column-integrated radiative and convective heating rates for the two MJOs and comparing them to the normalized gross moist stability (Neelin and Held 1987; Raymond et al. 2009; Sobel and Maloney 2012, 2013). Further work is underway to relate the budget results to cloud populations as determined by the research radars, but that effort is awaiting additional quality control and evaluation of the radar products.

2. Data and analysis procedures

a. Sounding observations

The DYNAMO sounding network was composed of two quadrilateral arrays—one north and one south of the equator—referred to as the northern and southern sounding arrays or NSA and SSA, respectively (Fig. 1).
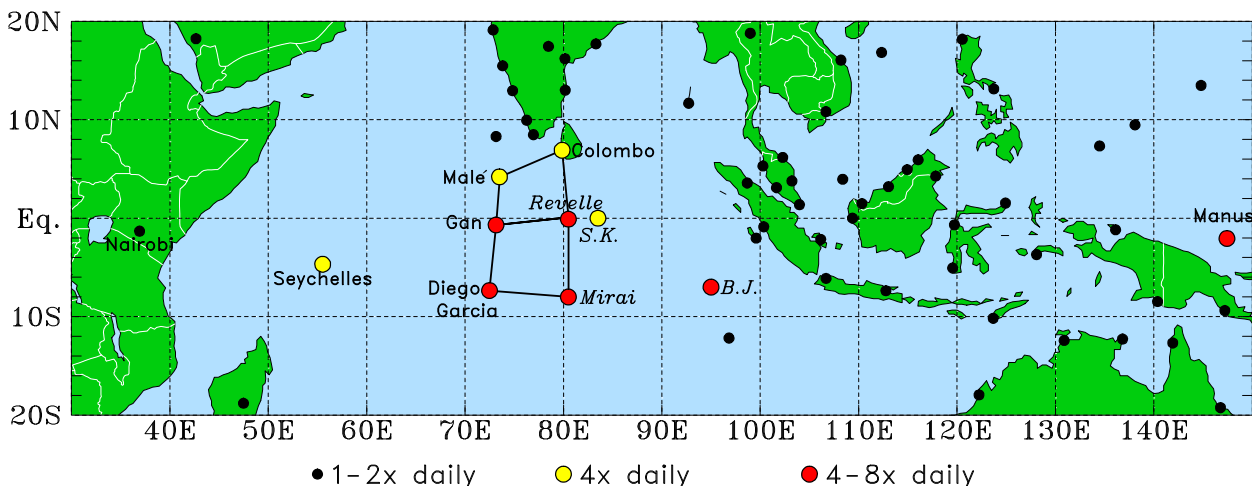
FIG. 1. DYNAMO–CINDY–AMIE sounding network for the period October–December 2011. Analysis domain includes high-frequency soundings (4 and 8 day^{-1}; yellow and red dots, respectively) and operational sounding sites (1 or 2 day^{-1}; black dots). Data from R/V *Sagar Kanya* (*S. K.*) and R/V *Baruna Jaya* (*B. J.*), which were on station for brief periods (25 Sep–19 Oct for *S. K.* and 5–18 Dec for *B. J.*), were also utilized in the analyses. Sites with enhanced sounding frequency during the SOP are labeled.

Details of the sounding systems, observing characteristics, and quality-control procedures are contained in Ciesielski et al. (2014a). Incorporated into our analyses are corrections for flow distortion and island heating effects by the mountainous island of Sri Lanka on Colombo soundings (Ciesielski et al. 2014b). Blockage of the low-level flow by the island terrain frequently disrupts the winds at Colombo below about 2 km. This local effect is aliased onto larger scales and impairs computations of divergence over the NSA. The procedure developed by Ciesielski et al. (2014b) mitigates the impacts of Sri Lanka flow blocking on budgets over the NSA by using European Centre for Medium-Range Weather Forecasts (ECMWF) Operational Analysis (OA) data away from the island to estimate what the wind, temperature, and moisture would be in the lowest 2 km at Colombo were the island not present.

The previous study of the thermodynamic and kinematic fields during the DYNAMO special observing period (SOP) (October and November 2011) by Johnson and Ciesielski (2013) was based on a preliminary version of the sounding data, which did not include corrections for humidity sensor biases at all sites. This study uses the complete set of corrections for humidity biases based on procedures described in Ciesielski et al. (2014a). In DYNAMO, Vaisala RS92 systems were used at five of the six SSA and NSA sites, while Colombo used a Meisei system. The humidity biases for the RS92s have been found to be relatively small—namely, daytime dry biases of ~2% in the lower troposphere and 5%–6% in the upper troposphere, which are only a third of the magnitude of the biases for the Vaisala RS80 sensors used in TOGA COARE (Wang et al. 2002; Ciesielski et al. 2003).

In addition to upsonde data, dropsonde data from the National Oceanic and Atmospheric Administration (NOAA) P-3 aircraft were incorporated into the gridded analyses described below. There were 469 dropsonde observations from 13 flights in proximity to the sounding arrays during the period 9 November–13 December.

To supplement conventional sounding winds, two sources of satellite winds were employed. First, surface winds over the ocean were obtained from the Advanced Scatterometer (ASCAT) on the *MetOp-A* satellite, which provides wind estimates nominally twice per day (0300–0600 and 1500–1800 UTC over the Indian Ocean) on a 12.5-km grid (Figa-Saldaña et al. 2002). To facilitate their use in our objective analysis, nonrain contaminated level 2 ASCAT winds were averaged into 3-h, 2.5° bins. In addition to these surface winds, we utilized upper-level atmospheric motion vector data derived from *Meteosat-7* visible, infrared, and water vapor data (Holmlund et al. 2001) produced by the Cooperative Institute of Meteorological Studies (CIMSS). For our analysis, these hourly wind vectors were averaged into 3-h, 25-hPa, 5°-resolution bins and used, only if at least three high-quality wind observations were present in a given bin. With this criterion, averaged satellite winds over the central Indian Ocean were available at 5° resolution >80% of the time for levels between 300 and 175 hPa and ~20% of the time for levels between 825 and 775 hPa with few observations at other levels.

Sounding thermodynamic data were supplemented with radio occultation (RO) profiles of T and T_d from the Constellation Observing System for Meteorology, Ionosphere and Climate (COSMIC) wetPrf product based on a 1D variational analysis using ECMWF analysis as a first

guess (Kuo et al. 2004). There were approximately 10 COSMIC profiles per month over each $5° \times 5°$ box over the Indian Ocean. Because of the well-documented negative refractivity bias in the tropical lower troposphere of RO soundings (Ao et al. 2003), no T_d information from this product was used below 850 hPa.

b. Other data sources

Precipitation rates derived from the sounding budgets are compared to estimates from several different sources. One is the Tropical Rainfall Measuring Mission (TRMM) 3B42v7 product, which combines microwave rainfall estimates from TRMM and other satellites with high-temporal-resolution infrared rain rate estimates to create a 3-hourly, $0.25° \times 0.25°$ rainfall dataset (Huffman et al. 2007). Other sources are the NOAA Climate Prediction Center (CPC) morphing technique (CMORPH) (Joyce et al. 2004), available on a 0.07° grid and at 30-min time resolution, the Global Precipitation Climatology Project (GPCP) with daily values on a 0.25° grid (Adler et al. 2003), and the Global Satellite Mapping of Precipitation (GSMaP) with hourly values on a 0.10° grid (Kubota et al. 2007; Aonashi et al. 2009).

Fractional cloudiness and radiation data are obtained from the Clouds and the Earth's Radiant Energy System (CERES) product at 3-hourly intervals on a 1° grid (Wielicki et al. 1996) and the Pacific Northwest National Laboratory (PNNL) Combined Retrieval (CombRet) product based on cloud and thermodynamic profile measurements at Gan Island (Feng et al. 2014). The CombRet product is only available from 10 October onward.

ECMWF OA at 0.25° horizontal resolution, 18 vertical levels from the surface to 50 hPa, and 6-hourly intervals are used to help constrain and extend the sounding-based analyses beyond the NSA and SSA domains. Unlike TOGA COARE, soundings outside the core DYNAMO area were extremely sparse, so such a procedure is needed to supplement the soundings. Furthermore, the ECMWF analyses were utilized to replace sounding data from ships when they were off station since the quality of the analyses is degraded when the network collapses from a quadrilateral to a triangle (Katsumata et al. 2011). Procedures for incorporating ECMWF OA in a way that enhances the analysis but minimally impacts derived fields such as divergence are described in the next subsection.

Surface fluxes and SST fields over the Indian Ocean are from the TropFlux product (daily values, 1° horizontal grid) based on Praveen Kumar et al. (2012). To check the reliability of the TropFlux data for DYNAMO, surface fluxes and SST from that product are compared to in situ measurements from the R/V Revelle, made available via

ftp://dynamo.dms.uconn.edu/ through a collaborative effort between NOAA/Earth System Research Laboratory (ESRL)/Physical Sciences Division, Oregon State University, and the University of Connecticut.

c. Data analysis procedures

While the sounding sites composing the SSA conducted 8-day^{-1} launches (Fig. 1), the two northern sites—Malé and Colombo—had a nominal launch frequency of 4 day^{-1}. Since there is a considerable interest in the diurnal cycle over both arrays (see Ruppert and Johnson 2015), the 6-hourly Malé and Colombo sounding data have been linearly interpolated in time to allow for budgets to be carried out at 3-hourly intervals over both the NSA and SSA. Interpolated soundings were only created if the time gap between soundings was less than or equal to the nominal 6-hourly sounding interval. The interpolation procedure was also used to fill in a handful of 6-h gaps in sounding data for the SSA. An evaluation of the impact of this procedure at Gan Island where 3-hourly soundings were taken throughout the experiment shows that the interpolation procedure results in relatively small errors. Specifically, rms differences in temperature, specific humidity, and winds between contemporaneous interpolated and actual soundings are ~0.5°C, 0.5 g kg^{-1}, and 1 m s^{-1}, respectively.

Owing to the large data-void regions outside the core sounding arrays, the ECMWF OA was used at 5° grid intersections if no observations (soundings, satellite winds, or otherwise) were present within a 4.5° radius of such an intersection. To facilitate its use at 3-h intervals, the ECMWF OA was linearly interpolated in time to create a 3-h-resolution product. Since this procedure to enhance data coverage was only applied outside the main core arrays, results in the interior are largely independent of model analyses and hence parameterizations of physical processes, as will be quantitatively demonstrated in section 6a. One exception is when ships were offsite, in which case model analyses filled in for missing ship soundings. Only during these periods did the model analyses noticeably impact budget quantities over the arrays. In recognition of the fact that the results have model influence during these periods, port-call intervals are specifically denoted in time series plots by shading or other designations.

Following interpolation to 3-hourly intervals, the sounding data, along with the other observations and model fields described above, were objectively analyzed onto a $1° \times 1°$ grid at the surface and at 25-hPa intervals from 1000 to 50 hPa over the entire domain shown in Fig. 1 using the multiquadric interpolation procedure as described in Ciesielski et al. (1997). Quality-controlled sounding data from sites shown in Fig. 1 outside the arrays were used to help constrain the analyses.

Corrections to the divergence were made such that vertical motion balanced to zero at the tropopause level (typically at 100 hPa), which was determined at each grid point and time step (Johnson and Ciesielski 2002).

3. Budget analysis considerations

Following Yanai et al. (1973), but including ice processes, we write the equations for the apparent heat source and moisture sink as follows:

$$Q_1 \equiv \frac{\partial \overline{s}}{\partial t} + \overline{\mathbf{v}} \cdot \nabla \overline{s} + \overline{\omega} \frac{\partial \overline{s}}{\partial p} = L_v(\overline{c} - \overline{e}) + (L_v + L_f)(\overline{d} - \overline{s}_*)$$

$$+ L_f(\overline{f} - \overline{m}) + Q_R - \frac{\partial}{\partial p}(\overline{s'\omega'}) \quad \text{and}$$

$$(1)$$

$$Q_2 \equiv -L_v\left(\frac{\partial \overline{q}}{\partial t} + \overline{\mathbf{v}} \cdot \nabla \overline{q} + \overline{\omega} \frac{\partial \overline{q}}{\partial p}\right)$$

$$= L_v(\overline{c} - \overline{e}) + L_v(\overline{d} - \overline{s}_*) + L_v \frac{\partial}{\partial p}(\overline{q'\omega'}), \quad (2)$$

where c, e, d, s_*, f, and m are condensation, evaporation, deposition, sublimation, freezing, and melting rates, respectively; q is the water vapor mixing ratio; $s \equiv c_p T + gz$ the dry static energy; Q_1 is the apparent heat source; Q_2 is the apparent moisture sink; Q_R is the net radiative heating rate; L_v and L_f are the latent heats of vaporization and fusion; an overbar refers to a horizontal average; primes refer a deviation from this average; and horizontal eddy flux divergences are assumed to be small.[1]

Integration of (1) and (2) from the tropopause pressure p_T to surface pressure p_0 yields

$$\langle Q_1 \rangle = \langle Q_R \rangle + L_v P_0 + \langle L_f(\overline{d} - \overline{s}_*)\rangle$$

$$+ \langle L_f(\overline{f} - \overline{m})\rangle + S_0 \quad \text{and} \quad (3)$$

$$\langle Q_2 \rangle = L_v(P_0 - E_0), \quad (4)$$

where $\langle \cdot \rangle \equiv 1/g \int_{p_T}^{p_0}(\cdot)\, dp$, the surface precipitation rate is $P_0 = \langle \overline{c} - \overline{e} + \overline{d} - \overline{s}_* \rangle$, S_0 is the surface sensible heat flux, and E_0 is the surface evaporation rate. In the following analysis, it is assumed that over the large sounding arrays and long time scales considered the terms $\langle L_f(\overline{d} - \overline{s}_*)\rangle$ and $\langle L_f(\overline{f} - \overline{m})\rangle$ in (3), for which there are no direct measurements, are comparatively small. Therefore, we

make the following approximation, as in Yanai and Johnson (1993):

$$\langle Q_1 \rangle \cong \langle Q_R \rangle + L_v P_0 + S_0. \quad (5)$$

As a check on this assumption, the Goddard cumulus ensemble modeling results of Tao et al. (2003) applied to the convectively active periods of the South China Sea Monsoon Experiment (SCSMEX) give a ratio of $\langle L_f(\overline{d} - \overline{s}_*)\rangle$ to $L_v P_0$ in (3) of ~0.03, while the ratio of $\langle L_f(\overline{f} - \overline{m})\rangle$ to $L_v P_0$ is far smaller.

Locally, however (e.g., averaged separately over the convective and stratiform regions of a tropical squall line), the above omitted terms are not negligible. These terms could also be important when there is a substantial buildup or decay in precipitation systems, even over large areas. For example, as convection builds up within the NSA during the developing phase of the MJO, there could be considerably more deposition than sublimation, as well as more freezing than melting, during a time interval of days, with the opposite being true during a decay phase. The latter situation is related to hydrometeor storage, which can be important on diurnal time scales (McNab and Betts 1978) or when the cloud volume is changing rapidly and/or when there is an advection of hydrometeors into or out of a region. An attempt was made by Johnson (1980) to estimate hydrometeor storage effects for a composite easterly wave during the GARP Atlantic Tropical Experiment, but determination of the evolving cloud and precipitation fields posed serious challenges and the computations contained considerable uncertainty. While we have future plans to utilize satellite, radar, and other data to investigate such storage effects, they are excluded from this study.

Defining moist static energy as $h \equiv s + L_v q$, subtraction of (2) from (1) and integration from the tropopause to any level p (neglecting the terms involving L_f) yields an expression for F, the vertical eddy flux of h:

$$F(p) \equiv -\frac{1}{g}\overline{(h'\omega')}_p \cong \frac{1}{g}\int_{p_T}^{p}(Q_1 - Q_2 - Q_R)\, dp, \quad (6)$$

or upon integration to the surface, we have following Yanai et al. (1973):

$$F_0 \equiv F(p_0) = S_0 + L_v E_0 \cong \langle Q_1 \rangle - \langle Q_2 \rangle - \langle Q_R \rangle. \quad (7)$$

An alternate version of (7) can be written as

$$\left\langle \frac{\partial \overline{h}}{\partial t}\right\rangle + \langle \overline{\mathbf{v}} \cdot \nabla \overline{h}\rangle + \left\langle \overline{\omega} \frac{\partial \overline{h}}{\partial p}\right\rangle$$

$$= \langle Q_1 \rangle - \langle Q_2 \rangle \cong S_0 + L_v E_0 + \langle Q_R \rangle. \quad (8)$$

---

[1] A more accurate representation of the moist thermodynamics includes conservation equations for vapor and airborne condensate, precipitation mass, and the entropy of moist air (e.g., Ooyama 1990). However, owing to the lack of direct measurements of microphysical processes and precipitation rates over the sounding arrays, we use the formulation of Yanai et al. (1973).

Sobel et al. (2014) used (8) along with the sounding data employed in this study and also Interim ECMWF Re-Analysis (ERA-Interim) data to investigate the moist static energy budget for the October and November MJOs. That analysis will not be repeated here, but we will relate our findings to theirs where appropriate.

The above set of equations can be used to check the accuracy of the budgets. The surface precipitation rate P_0 can be estimated from the moisture or heat equations, (4) or (5), but since $\langle Q_R \rangle$ is not directly measured, and (5) is an approximation, we use (4), with E_0 from TropFlux, to compute P_0 and compare those values with independent satellite-based estimates for the sounding arrays.

We use (7) to compute $\langle Q_R \rangle$, again using surface fluxes from TropFlux, and compare these values with independent estimates from CERES (for the arrays) and PNNL (for Gan Island). Following the procedures in Johnson and Ciesielski (2000), we also include several additional effects, which act in the direction to increase, albeit slightly, the diagnosed radiative cooling rate. They are: 1) the effects of mass sources and sinks resulting from precipitation and surface evaporation on the computation of vertical motion (Trenberth 1991); 2) the sensible heat flux due to rain, which falls at the wet-bulb temperature (Gosnell et al. 1995); and 3) frictional dissipation associated with falling precipitation (Emanuel and Bister 1996).

In past budget studies, we did not have sufficient information on the vertical structure of Q_R to compute the vertical profile of F. For DYNAMO, however, we have the PNNL CombRet product that provides the vertical profile of Q_R (Feng et al. 2014), so $F(p)$ can be computed. Unfortunately, cloud measurements taken at the AMIE site on Gan Island undersampled high-level cirrus clouds owing to signal attenuation in heavy rainfall, so their effects are not fully represented in the CombRet radiative heating rates. As a result, the CombRet net tropospheric radiative cooling during the cirrus-abundant convectively active phase of the MJO is somewhat overestimated compared to the CERES product, as will be shown later. Therefore, for the computation of F, we adjust the profile of Q_R from CombRet by a constant fraction at each level so that its vertical integral matches that of the CERES product. Ideally, this adjustment should be distributed vertically in a realistic way, but we do not have sufficient information to do so at this time.[2]

---

[2] In addition to the cirrus cloud issue, it has been pointed out to the authors by Adam Sobel that the lower boundary for the surface longwave flux in CombRet was taken to be land, which is unrepresentative of the surrounding ocean and differs from the corresponding CERES value by several tens of watts per square meter.

4. Broadscale distributions of rainfall

a. Surface flux estimates used in rainfall computations

Computations of precipitation and radiative heating rates over the arrays rely on estimates of surface fluxes over the enclosed areas. Two flux products have been tested: the Woods Hole Oceanographic Institution (WHOI) objectively analyzed air–sea fluxes (OAFlux) based on Yu and Weller (2007) and TropFlux (Praveen Kumar et al. 2012). Similar results were obtained for both products; however, since TropFlux yields slightly better agreement with the latent heat flux with measurements at the Revelle and slightly better correlations of computed rainfall rates to those observed, we employ that product for the following analyses.

To evaluate the accuracy of TropFlux for DYNAMO, surface fluxes from that product are compared to bulk fluxes at the Research Vessel (R/V) Revelle computed using the COARE 3.0 algorithm (Fairall et al. 1996). The mean of TropFlux values that fall within a 1° radius of Revelle's nominal position are plotted in Fig. 2 along with daily averaged Revelle fluxes when the ship is on station. SST from the Revelle are also shown in Fig. 2, as is the mean TRMM rainfall within the 1° radius of the site. The surface sensible and latent heat fluxes and SST, both the daily and SOP-mean values, show generally good agreement throughout much of the period, although there are occasions of disagreement (e.g., the SST in mid-November). Part of the disagreement is likely related to the fact that one data source (Revelle) is a point measurement and the other (TropFlux) is an area measurement. SOP-mean values of S_0, $L_v E_0$, and SST are 10–11 W m^{-2}, 106–107 W m^{-2}, and 29.5°C, respectively. These values are in close agreement with those reported over the western Pacific during TOGA COARE (Weller and Anderson 1996).

b. Large-scale temporal and spatial distributions of rainfall

Using surface latent heat fluxes over the Indian Ocean from TropFlux, 3-day running-mean filtered, daily average rainfall rates computed from (4) are compared to TRMM 3B42 estimates (3-hourly, unfiltered) in Fig. 3. In the longitude band of the sounding arrays (72°–80°E), the analysis is based on the sounding data whereas, outside the arrays, it is based principally on the ECMWF OA. Though peak amplitudes in the moisture budget rainfall are reduced by the filtering, the spatial and temporal distribution of budget estimates agree well with the TRMM envelopes of convection for the two MJO events in October and November. This filtered version of the budget analysis does not capture the higher-frequency disturbances embedded within the MJOs (Gottschalck et al. 2013), such as the 2-day disturbances within the active phase of
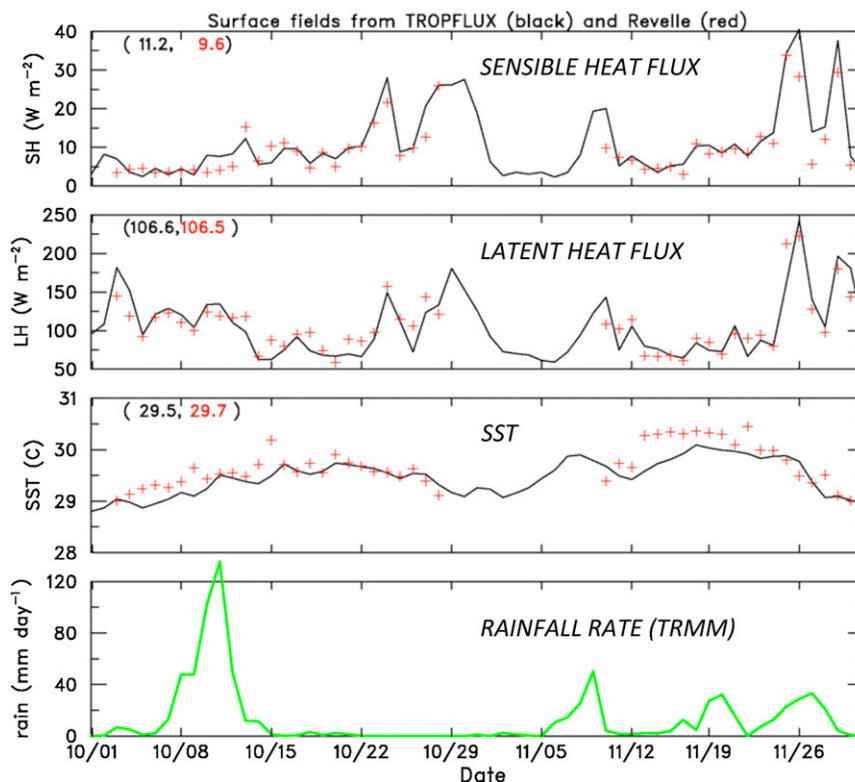
FIG. 2. (top to middle bottom) Time series of daily averaged sensible and latent heat fluxes (W m^{-2}) and SST (°C) from TropFlux (black curves: means within 1° radius of *Revelle's* nominal position) and the R/V *Revelle* (red pluses). Mean values for TropFlux (black) and the *Revelle* (red) are in parentheses at the top of each of the three panels. (bottom) Average rainfall rate (mm day^{-1}) within a 1° radius of *Revelle* nominal position (0°, 80.5°E) from TRMM 3B42.

the MJO in October (Zuluaga and Houze 2013; Johnson and Ciesielski 2013). Analyses of the heat and moisture budgets for these disturbances are left for future work.

A broadscale depiction of the SOP-mean rainfall rate over the Indian Ocean for October and November is presented in Fig. 4. Rainfall rate diagnosed from the moisture budget is in overall good agreement with the TRMM estimates both in terms of magnitude and areal distribution. A prominent feature of the rainfall pattern is an ITCZ-like band between the equator and 10°S extending across much of the Indian Ocean. Slightly greater SOP-mean rainfall rates can be seen over the SSA than the NSA in both TRMM (9.1 vs 8.9 mm day^{-1}) and the budgets (10.6 vs 9.4 mm day^{-1}).

5. Heat and moisture budgets for sounding arrays

a. Time series for SOP

Time series of the apparent heat source Q_1 and apparent moisture sink Q_2 over the NSA for October and November are shown in Fig. 5 along with NSA daily

mean rainfall from TRMM. The MJO heavy-rain periods in the latter half of both months are accompanied by pronounced increases in the amplitudes of Q_1 and Q_2. It should be noted that, as expected, the rainfall time series for the entire NSA shown in Fig. 5 does not correlate well with that for a single location—namely, at the *Revelle* (Fig. 2)—but it does represent well the convectively active periods of the October and November MJOs (Fig. 3).

The evolution of Q_1 and Q_2 through both MJO events (Fig. 5) shows a similar progression to that observed during TOGA COARE (Lin and Johnson 1996): shallow, nonprecipitating cumulus indicating lower-tropospheric moistening (negative Q_2) during the suppressed periods (RMM phases 6–8 and the early portion of 1), followed by cumulus congestus (low-to-midlevel peaks in Q_1 and Q_2 in RMM phase 1 and early part of 2), then deep convection (higher peaks in Q_1 and Q_2 in RMM phases 2 and 3), and finally stratiform-like profiles of Q_1 and Q_2 (positive values aloft, negative at low levels in RMM phases 3 and 4). This
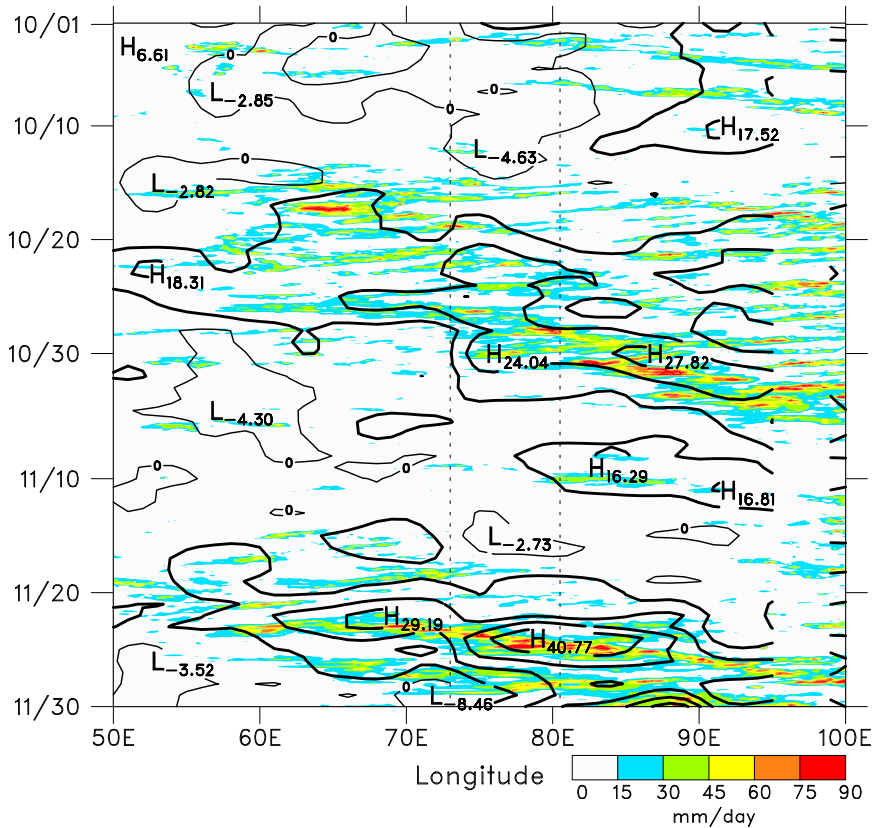
FIG. 3. Time–longitude plot of rainfall rates from TRMM 3B42 (3-hourly values, color) and moisture budget (3-day running-mean filtering of daily average values, contours, mm day^{-1}) averaged over 5°N–5°S for DYNAMO SOP. The vertical dashed lines denote the east and west boundaries of sounding arrays. Missing moisture budget results between 95° and 100°E mark location of Sumatra, where surface flux data do not exist.

progression is consistent with now generally accepted paradigm for the evolution of precipitation systems and diabatic heating through the life cycle of the MJO (Johnson et al. 1999; Kiladis et al. 2005; Zhang 2005; Mapes et al. 2006; Benedict and Randall 2007; Haertel et al. 2008). A notable difference between the two events, however, is the longer duration of both the buildup and convectively active periods for the October MJO compared to the November MJO. In addition, the convective moistening by shallow cumulus during the suppressed periods was stronger for the October than the November event. It is also noted that the maxima in heating and drying in Fig. 5 are coincident with peaks in NSA-averaged TRMM rainfall, both in connection with the 2-day disturbances in late October (Zuluaga and Houze 2013) and the two Kelvin waves in November. This correspondence between the Q_1 and Q_2 peaks and rainfall lends confidence to the budget results for DYNAMO.

There has been evidence from past studies of a stepwise progression of the cloud fields from shallow cumulus to congestus to deep convection (Kikuchi and Takayabu 2004; Yoneyama et al. 2008; Virts and Wallace 2010; Del Genio et al. 2012) as well as in preliminary results from DYNAMO itself in high-resolution time series of relative humidity at Malé, Gan Island, and the R/V *Revelle* (Fig. 13 of Johnson and Ciesielski 2013). The results in Fig. 5 are suggestive of a similar behavior; namely, there are approximately 5-day periods (15–20 October and 17–22 November) of low-to-midtroposphere heating and drying conceivably associated with cumulus congestus populations. This relationship will be further explored in terms of the eddy fluxes of moist static energy F later in section 8. However, definitive conclusions regarding stepwise evolution of cloud populations will have to await further work integrating sounding budget findings with research radar observations, which is beyond the scope of the present study.

The time series of Q_1 and Q_2 over the SSA (Fig. 6) contrasts markedly to that over the NSA even though both arrays share the common sites Gan Island and
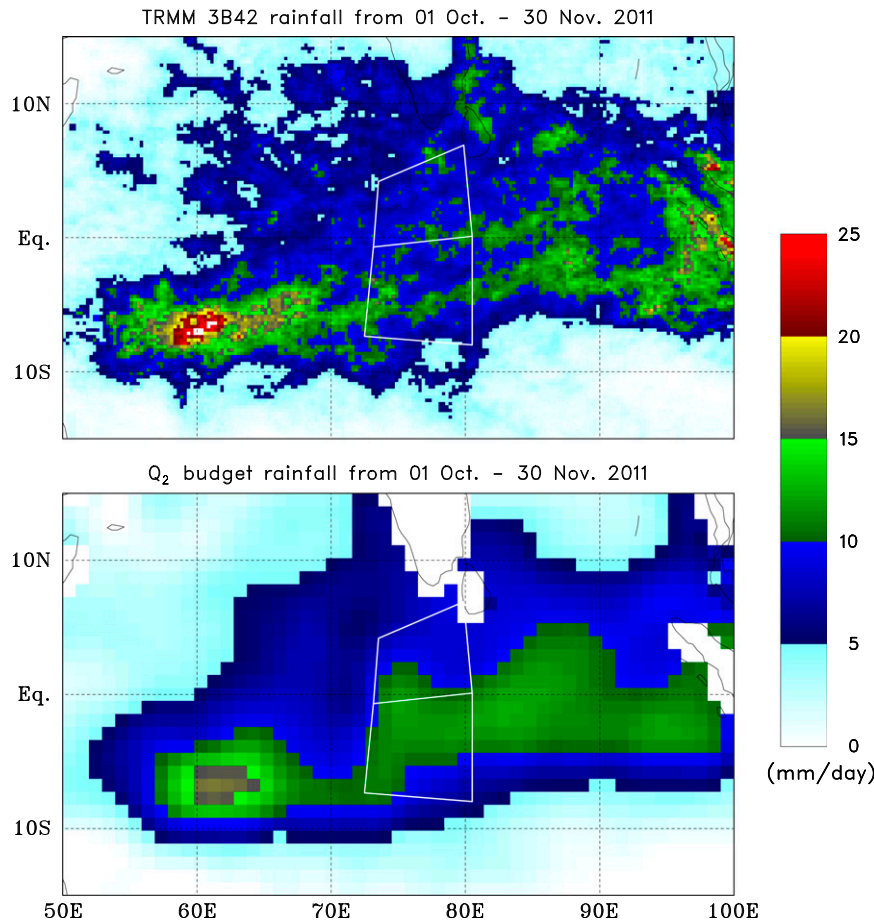
FIG. 4. Mean rainfall rate (mm day^{-1}) over Indian Ocean for October–November 2011 from (top) TRMM 3B42 product and (bottom) moisture budget. White lines denote sounding arrays. Budget rainfall not computed over land owing to the absence of surface flux data there.

Revelle. As noted in Johnson and Ciesielski (2013), the MJO signal during the October–November period of DYNAMO was stronger north of the equator during this boreal fall period. Frequent episodes of rainfall corresponding to periods of heating/drying occurred throughout the 2-month period with a moderate increase in convective activity associated with the MJOs toward the ends of October and November. As can be seen from Fig. 4, the SSA straddled an ITCZ-like band of precipitation between the equator and 10°S, which is reflected in the semipermanent precipitation in that array.

b. Mean profiles for SOP

SOP-mean vertical profiles of Q_1 and Q_2 for the NSA and SSA, along with frequency–altitude diagrams for each, are shown in Fig. 7. The amplitudes of the profiles are similar between the two arrays, consistent with the approximate agreement in TRMM 3B42-estimated

rainfall for the NSA (8.9 mm day^{-1}) and SSA (9.1 mm day^{-1}). The Q_1 and Q_2 profile shapes are similar over the NSA, while the peaks are widely separated over the SSA. These results suggest a greater fraction of stratiform precipitation over the NSA than the SSA (e.g., Luo and Yanai 1984). This inference is supported by the frequency–altitude diagrams for the NSA (Fig. 7), which show a greater spread of negative Q_2 values (indicative of moistening by evaporation) and a higher frequency of negative Q_1 values (cooling) in the lower troposphere (between 900 and 600 hPa) than for the SSA.

Three research radars were deployed in DYNAMO, but their precipitation area coverage is a small fraction (~8%–9%) of the areas of the sounding arrays, so they cannot be used to check the inference of greater stratiform rain fraction over the NSA. Analysis of the convective–stratiform fractions from the TRMM 2A25 product does show a greater stratiform fraction for the NSA (55%) than
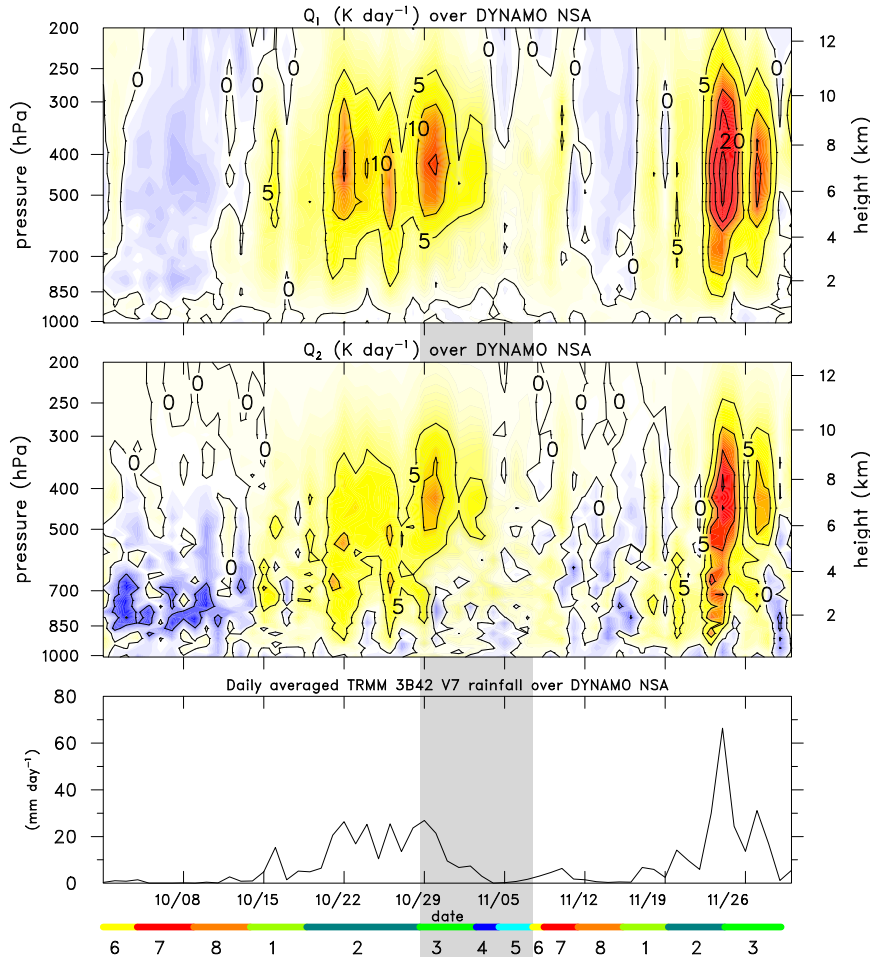
FIG. 5. Time series for October and November of daily average values of (top) apparent heat source Q_1 (K day^{-1}), (middle) apparent moisture sink Q_2, and (bottom) TRMM 3B42v7 rainfall rate (mm day^{-1}) for NSA. Wheeler and Hendon (2004) RMM index shown below bottom panel. Shaded bar denotes port-call period for R/V *Revelle*.

the SSA (50%), although the sampling for the 2-month period is limited. In particular, there were 102 (117) TRMM overpasses for the NSA (SSA) during the SOP; nevertheless, the 5% difference is significant at the 95% level using a one-sided Student's *t* test. These TRMM stratiform fractions are greater than the tropical global estimate of ~40%,[3] although the TRMM climatologies of Schumacher and Houze (2003) and Funk et al. (2013) show higher values (by about 5%) over the central Indian Ocean. Recent analyses of the SMART-R radar data on Gan Island by DePasquale et al. (2014) indicate a mean stratiform rain fraction of 41% for what they refer to as

the active periods of the October, November, and December MJOs. Despite the disagreement in magnitudes, the TRMM estimates for DYNAMO do show a greater stratiform contribution to rainfall over the NSA than the SSA, which is consistent with the budget findings. Considering that the MJO signal was stronger over the NSA than the SSA (Johnson and Ciesielski 2013), these findings are also consistent with the results of Lin et al. (2004) that indicate a greater stratiform rain fraction within the MJO convective envelope than the tropical mean.

6. Precipitation rate intercomparisons

a. Impact of ECMWF operational analysis data on budgets

As noted earlier, the ECMWF OA has been used outside the sounding arrays but also in proximity to the

---

[3] This estimate was recently revised downward to ~35% by Funk et al. (2013) based on a consideration of misclassification of some shallow clouds as stratiform in the TRMM 2A23v7 algorithm. Similar downward adjustments are likely needed for the DYNAMO estimates for the NSA and SSA.
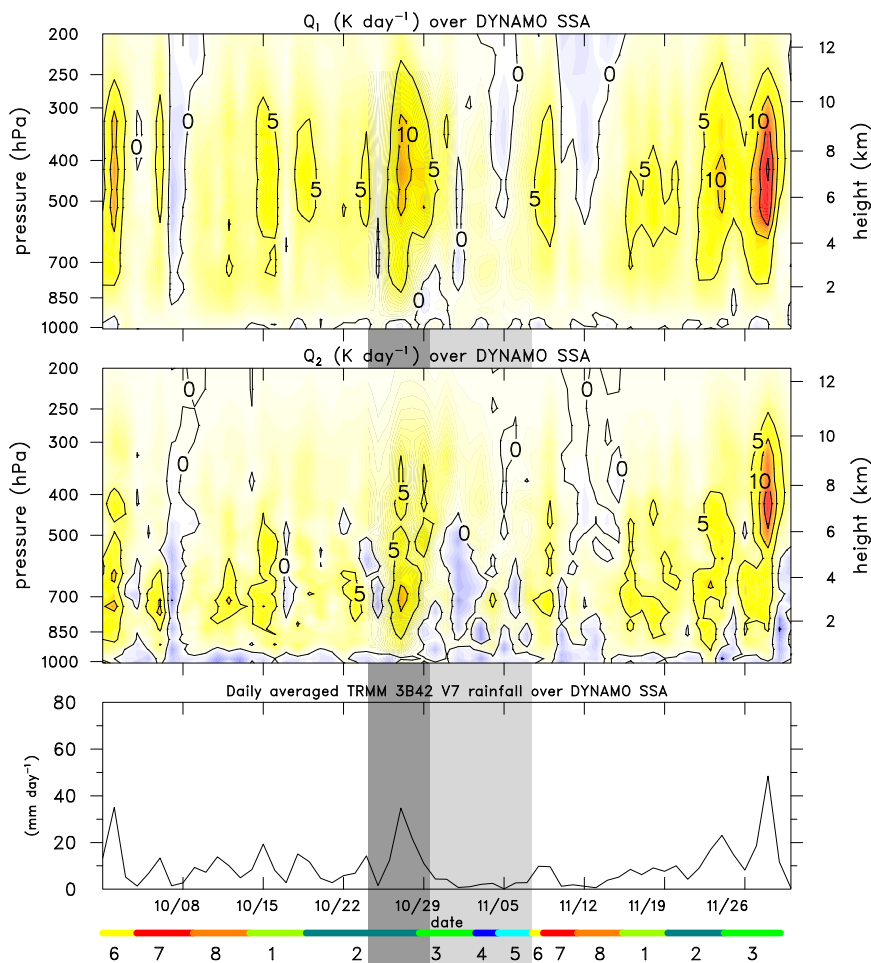
FIG. 6. As in Fig. 5, but for SSA. Dark and light vertical shaded bands indicate times when R/V *Mirai* and *Revelle*, respectively, were off station.

R/Vs *Revelle* and *Mirai* when those ships were off station in order to improve the analyses during the port-call periods. To demonstrate this improvement, and to also show the minor effects of the model analyses at other times, a time series of rainfall rate computed from the Q_2 budget for the NSA with and without ECMWF analyses is shown in Fig. 8 (top panel). Outside the port-call period, there is mostly only a minor change in the rainfall estimates by the inclusion of ECMWF OA (Fig. 8, bottom panel), supporting the assertion of minimal impact of model analyses when all sites were occupied. A similar comparison of the divergence profiles (not shown) indicates little impact by the model analyses during that period. Overall, the budget and TRMM rainfall rates agree well, and the agreement during the port-call period improves with the inclusion of ECMWF OA (values are generally overestimated without ECMWF OA). Averaged over the entire SOP, the addition of ECMWF OA brings the NSA mean budget rainfall rate (9.4 mm day^{-1})

more in line with the TRMM estimate (8.9 mm day^{-1}). The budget estimate for the NSA area and for the 2-month period corresponding to the SOP is subject to a random sampling error of 0.3 mm day^{-1} based on the work of Mapes et al. (2003).

b. Intercomparison of budget and satellite estimates

A comparison between the budget rainfall estimates and those for four different satellite products is shown in Fig. 9 and Table 1 for both the NSA and SSA. There is good agreement among the various satellite products and the budgets for the NSA: satellite estimates ranging from 8.9 to 9.8 mm day^{-1} compared to the budget 9.4 mm day^{-1}. The agreement is slightly poorer for the SSA: 8.2 to 9.7 mm day^{-1} compared to the budget 10.6 mm day^{-1}. For the NSA, temporal correlations between budget estimates and TRMM, CMORPH, GPCP, and GSMaP (all with 3-day running-mean filtering of daily average values) are 0.97, 0.96, 0.93, and 0.93,
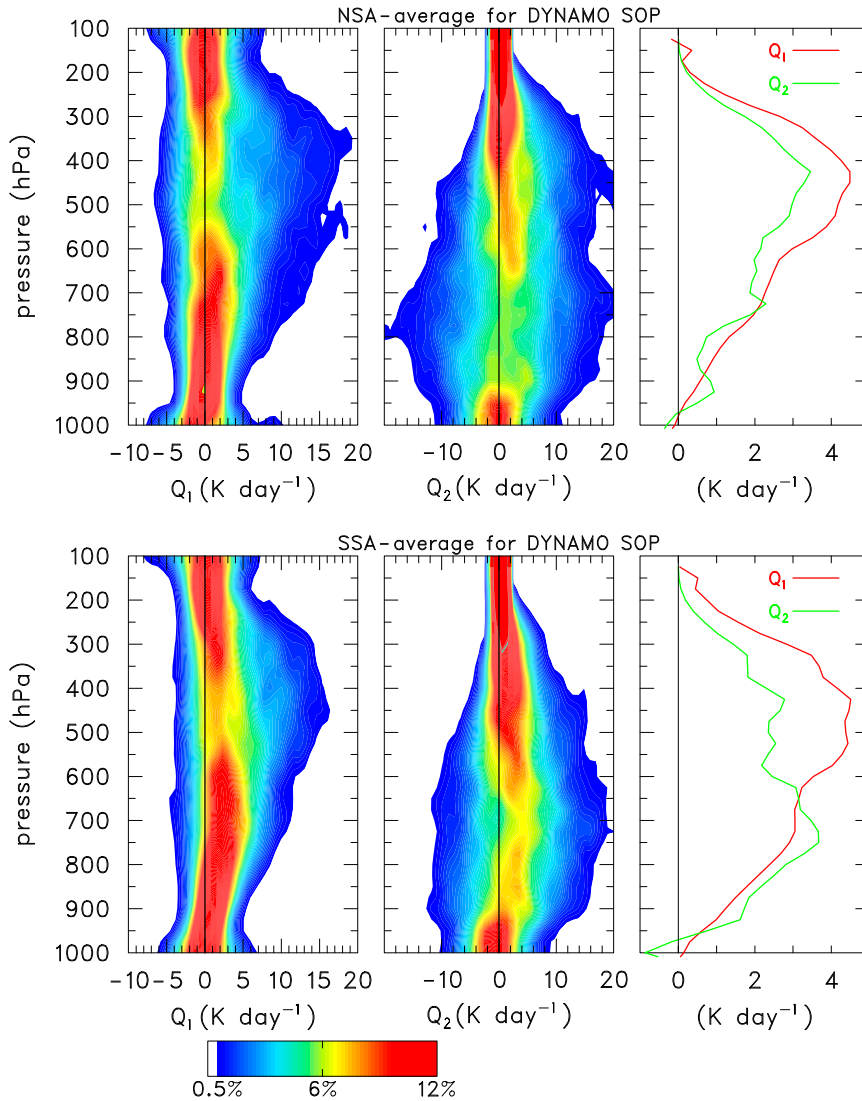
FIG. 7. (left),(center) Frequency–altitude distributions and (right) SOP-mean profiles of Q_1 and Q_2 for (top) NSA and (bottom) SSA for October–November 2011.

respectively. The correlations for the SSA are not quite as good: 0.92, 0.90, 0.82, and 0.86, respectively, for the same products; nevertheless, the correlations for both the NSA and SSA are significant at the 99% level using a one-sided Student's t test. For both the NSA and the SSA, the budget estimates exceed the satellite estimates during much of the suppressed phases (most of RMM phases 8 and 1, as well as 7 in November) while the opposite is true during the MJO convectively active phases (much of RMM phases 2 and 3). Using shipborne radar data from the *Revelle*, Xu and Rutledge (2014) show that the TRMM 3B42 product, which is based on a combination of microwave and infrared data, underestimates rainfall during suppressed periods, presumably owing to insufficient sampling of shallow, warm-rain cells, while it overestimates

rainfall during the convectively active phases, likely owing to the abundance of high-level cloudiness at those times. These deficiencies in the satellite products are in the right direction to explain at least some of the differences between the budgets and satellites in Fig. 9. The fact that there is a greater discrepancy for the SSA (budgets exceeding the satellite estimates) may be related to the more frequent occurrence in the SSA of light-to-moderate rain episodes, when satellites tend to underestimate rainfall, and weaker, briefer heavy-rain episodes associated with the MJOs, when the high-level cloud coverage and stratiform rain fractions are higher (Barnes and Houze 2013; Powell and Houze 2013; DePasquale et al. 2014) and satellites tend to overestimate rainfall (Liu et al. 2007; Xu and Rutledge 2014).
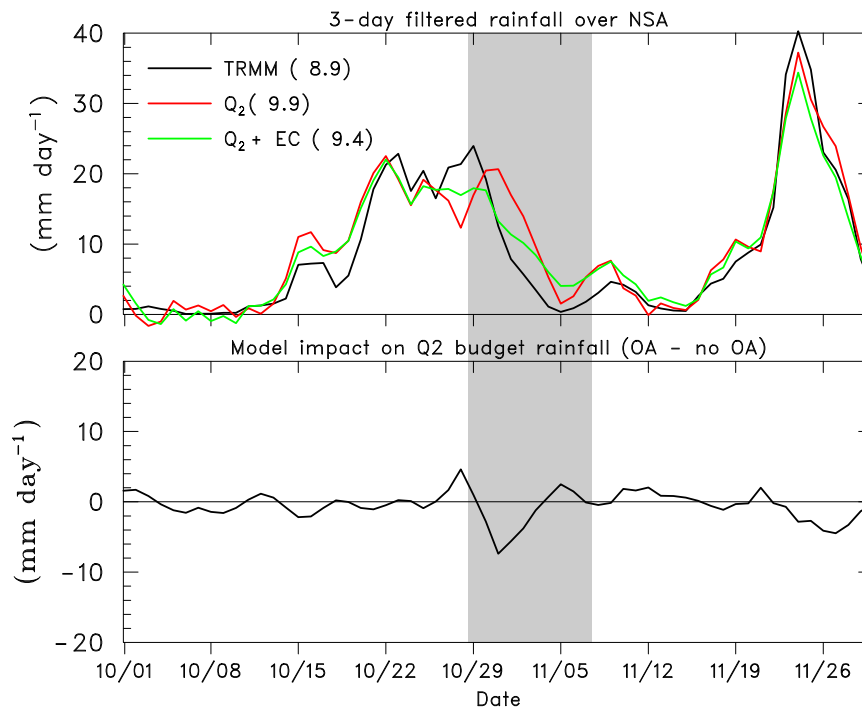
FIG. 8. SOP time series (filtered, 3-day running mean) for NSA of (top) rainfall rate (mm day^{-1}) computed from Q_2 budget with (green curve) and without (red curve) inclusion of ECMWF OA with comparison to TRMM 3B42v7 data (black curve), and (bottom) changes to Q_2 budget resulting from inclusion of model reanalyses. Numbers in parentheses in top panel refer to SOP-mean rainfall rate. Shading denotes period of R/V *Revelle* port call.

The mean NSA budget rainfall rate for the DYNAMO SOP (9.4 mm day^{-1}) is comparable to the mean value of 8.4 mm day^{-1} for the 4-month intensive observing period (IOP) of the TOGA COARE Intensive Flux Array (IFA) (Table 1). The correlations between the budget and satellite-based rainfall estimates for DYNAMO, all exceeding 0.90 for the NSA, represent an improvement over the TOGA COARE IFA budget and satellite rainfall rate correlations that were closer to 0.80 (Ciesielski et al. 2003).

Also seen in Fig. 9 are the possible effects of hydrometeor storage on the budgets (McNab and Betts 1978; Johnson 1980), particularly over the NSA for the October MJO. During the period of increasing precipitation between 15 and 22 October, the budget rainfall rate exceeds all of the satellite estimates, but the reverse is true toward the end of October. The discrepancy for the 15–22 October period may be related to the storage of water in clouds as the cloud area increased rapidly (as shown in the next section), whereas the reverse situation at the end of the month is presumably a result of evaporation of cloud systems generated at an earlier time as the cloud area decreased rapidly. Evidence of storage effects is not as obvious for the November MJO. Determination of cloud storage effects is complicated, requiring estimates

of changing cloud volumes within the arrays, cloud water mixing ratios, etc., and is beyond the scope of the present study.

7. Intercomparison of radiative heating rates

a. Budget–satellite intercomparisons, relationship to cloud cover

In this section we compare $\langle Q_R \rangle$ obtained from the combined heat and moisture budgets and surface fluxes (7) with the CERES and PNNL radiation products. However, we first show a time series of the vertical profile of daily averaged Q_R from the PNNL CombRet product for Gan Island (Feng et al. 2014), along with 3-month-mean values of shortwave, longwave, and net radiative heating (Fig. 10). The October and November MJOs are clearly seen to modulate Q_R, as does another MJO-like event in December described by Gottschalck et al. (2013) and Yoneyama et al. (2013). During the convectively active phases in the latter halves of the months, greatly reduced net radiative cooling, even reverting to a net heating at times, is seen to occur in the midtroposphere (800–400 hPa) in response to the increased upper-level cloud cover (shown later). In the upper troposphere
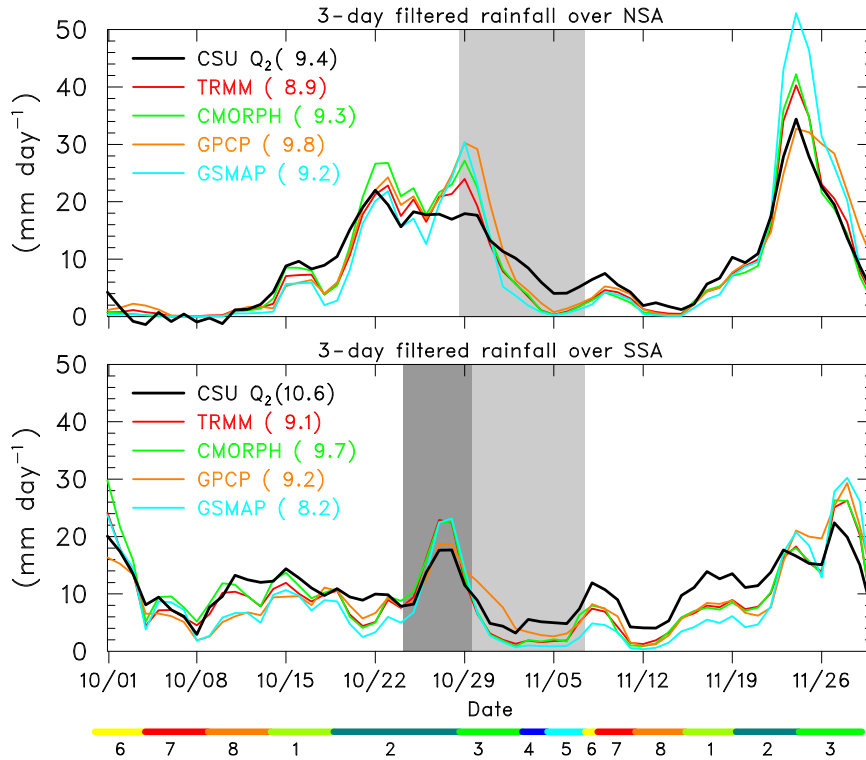
FIG. 9. SOP time series of 3-day running-mean filtered rainfall rate (mm day^{-1}) computed from Q_2 budget (with ECMWF OA included) compared to TRMM 3B42v7, CMORPH, GPCP, and GSMaP estimates for (top) NSA and (bottom) SSA. Numbers in parentheses refer to SOP-mean rainfall rates. Light (dark) shading denotes periods of R/V *Revelle* (*Mirai*) port calls. RMM index shown below bottom panel.

between 400 and 200 hPa, intermittent enhanced cooling can be seen, reflecting increased longwave cooling atop upper-level cloud systems. However, the overall cooling in this layer is likely overestimated owing to the undersampling of cirrus clouds by the instrumentation on Gan Island (Feng et al. 2014). This conclusion is supported by the study of Jiang et al. (2011), which shows a similar modulation of Q_R by the MJO from the TRMM-based radiation algorithm of L'Ecuyer and McGarragh (2010), but the maximum heating (i.e., minimum cooling) during the convectively active phases is shifted upward to near 300 hPa as opposed to the peaks being centered more in the midtroposphere in the CombRet product. The weak heating near 100 hPa is attributable to localized heating in the 15-μm CO_2 band owing to the sharp curvature in the temperature profile (Thuburn and Craig 2002). The mean profile of Q_R shows a ~1 K day^{-1} net cooling averaged through the troposphere, with slightly greater cooling near the surface and in the upper troposphere.

SOP time series of $\langle Q_R \rangle$ from the budgets and other independent estimates for the NSA and SSA, along with SOP-mean values, are shown in Fig. 11 and Table 1. The budget and CERES results are for the array areas, while the CombRet estimate is for the Gan Island location only. Two curves are shown for the budget results: one with the inclusion of the effects of precipitation/ evaporation on the computation of divergence, sensible heat flux due to rain, and frictional dissipation associated with precipitation (solid black curve) and one without (dashed black curve). These effects are minor, but they bring the period-mean $\langle Q_R \rangle$ values, -0.59 and -0.53 K day^{-1}, into closer agreement with the CERES SOP-mean values, -0.63 and -0.62 K day^{-1}, for the NSA and SSA, respectively (Table 1). The CERES SOP-mean $\langle Q_R \rangle$ for the Gan Island location is -0.60 K day^{-1}, which is very close to the NSA- and SSA-mean values. For the array areas and 2-month period of the SOP, the random sampling error for $\langle Q_R \rangle$ associated with the budget results is 0.03 K day^{-1} (Mapes et al. 2003). In addition to the SOP-mean values, the temporal variability of the budget and CERES $\langle Q_R \rangle$ are in reasonable agreement, although there are certain periods (first half of October and late November) where the disagreement is large. The differences during these periods are not fully understood, although part of the explanation likely lies in the fact that the computation

TABLE 1. SOP-mean rainfall and radiative heating rates based on budgets and satellite estimates for DYNAMO NSA and SSA, as well as comparisons with 4-month budget averages for TOGA COARE IFA. Areas of arrays are also indicated.

Item	Source	DYNAMO NSA	DYNAMO SSA	COARE IFA
Areas		$(700 \, \text{km})^2$	$(830 \, \text{km})^2$	$(474 \, \text{km})^2$
Rainfall rates (mm day^{-1})				
	Q_2 budget	9.4	10.6	8.4
	TRMM	8.9	9.1	
	CMORPH	9.3	9.7	
	GPCP	9.8	9.2	
	GSMaP	9.2	8.2	
Tropospheric-mean radiative heating $\langle Q_R \rangle$ (K day^{-1})				
	Budgets without rain correction	−0.53	−0.46	
	Budgets with rain correction	−0.59	−0.53	−0.55
	CERES	−0.63	−0.61	

of $\langle Q_R \rangle$ from (8) involves a small difference between two large quantities ($\langle Q_1 \rangle$ and $\langle Q_2 \rangle$) and hence is also quite sensitive to S_0 and $L_v E_0$.

The budget-mean value of $\langle Q_R \rangle$ for the DYNAMO arrays is very close to the value of $-0.55 \, \text{K day}^{-1}$ obtained for the TOGA COARE IFA by Ciesielski et al. (2003) using the same budget methodology (Table 1). In addition, the large-amplitude variation of $\langle Q_R \rangle$ over the life cycles of the DYNAMO MJOs closely resembles that observed for the major December 1992 MJO event in TOGA COARE (Johnson and Ciesielski 2000). Past studies have shown that this horizontal variability can have substantial impacts on the tropical Walker and Hadley circulations (Hartmann et al. 1984; Slingo and Slingo 1988, 1991; Randall et al. 1989; Sherwood et al. 1994; Webster 1994; Raymond 2000). In addition, the reduction in radiative cooling (increase in column-integrated radiative heating) beginning in the middle of October and November as cirrus started to increase [also observed for the December MJO during TOGA COARE (Johnson and Ciesielski 2000)] could play an important role in the buildup of moist static energy prior to the active phases of the MJOs (Chikira 2014; Sobel et al. 2014). Qualitatively, the modulation of $\langle Q_R \rangle$ by the MJOs is similar in the CombRet estimate, though the SOP-mean net cooling rate ($-0.81 \, \text{K day}^{-1}$) is greater. This discrepancy is likely related in part to the undersampling of upper-tropospheric clouds by the instrumentation on Gan Island and, hence, exclusion of their full effects in the radiation calculations.

The time series of budget and CERES $\langle Q_R \rangle$ for the NSA are repeated in Fig. 12 (middle panel), but to better illustrate the full cycle of the November MJO, for a slightly longer period than the SOP (until 6 December when 6-hourly soundings on Colombo were terminated). Also included are a time series of relative humidity (top panel) and cloud fractional area from the CERES product for low, low-middle, high-middle, and high clouds (bottom panel). Figure 12 shows a strong correlation of the net tropospheric radiative heating with upper-tropospheric clouds—namely, $|\langle Q_R \rangle|$ decreases (increases) as the high clouds increase (decrease). This result confirms the important role of high-level clouds in trapping longwave radiation in the troposphere (e.g., Hartmann et al. 1992; Stephens et al. 1994). The fractional area of shallow clouds is seen to decrease during the convectively active phases of the MJO (Zuluaga and Houze 2013); however, there may be some blocking of the satellite detection of shallow clouds by upper-level cloud layers. There is a slight increase in middle-low cloud coverage in the middle of October and November, consistent with the implied increase in congestus activity during those times from the heat and moisture budgets (Fig. 5). Detailed comparisons of the budget results with cloud populations measured by the DYNAMO research radars are left for future study.

Also evident from Fig. 12 is an increase in upper-tropospheric relative humidity in the middle of each month, consistent with the increase in high-level clouds and a corresponding reduction in $|\langle Q_R \rangle|$ that occurred at those times. As noted in Johnson and Ciesielski (2013, their Fig. 11), this moistening was associated with a cool anomaly aloft (between 200 and 100 hPa) in mid-October in advance of the convectively active phase of the MJO. The tilted warm–cool anomaly pattern that was observed during DYNAMO (Johnson and Ciesielski 2013) resembled that first described by Kiladis et al. (2001), who explained this feature as a gravity wave response to the large-scale MJO convective heat source envelope. It is consistent with the recent findings of Virts and Wallace (2010) and Virts et al. (2010), who determined from an analysis of CALIPSO cirrus data that the coldest, cloudiest anomalies aloft occur ~30° east of the main MJO convective heat source and descend with time,
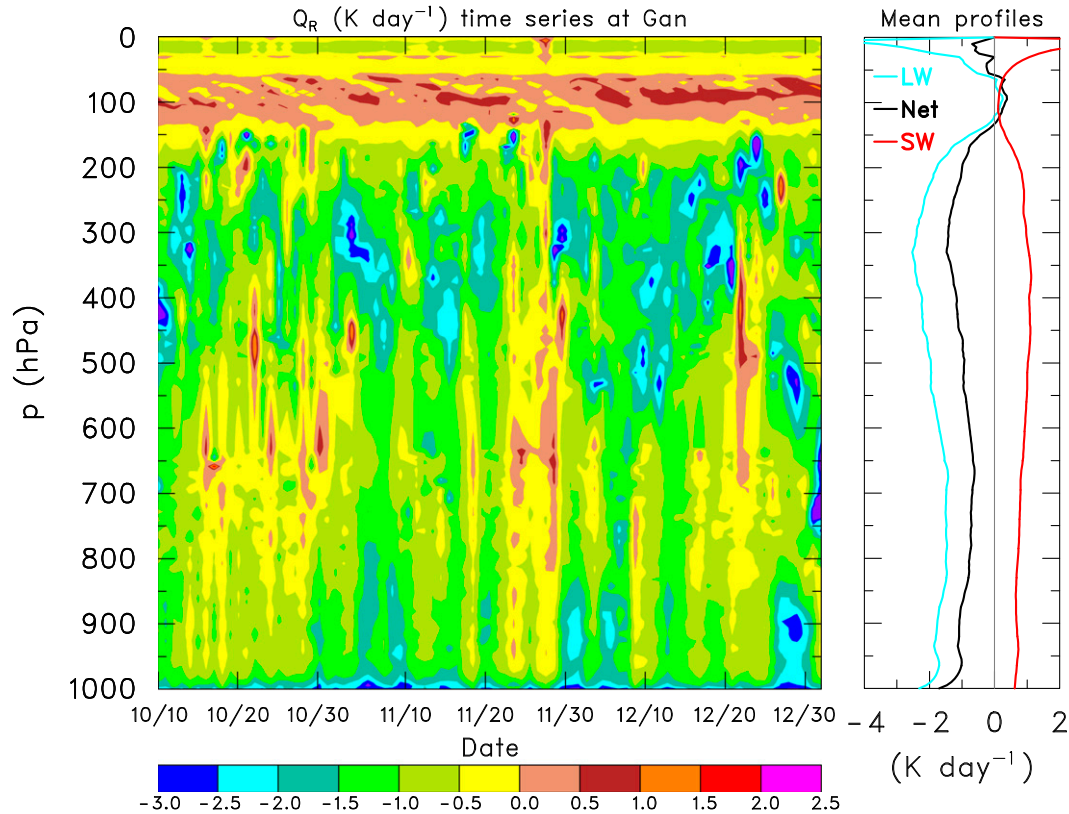
FIG. 10. (left) Time series of daily averaged net radiative heating rate (K day^{-1}) at Gan Island from PNNL CombRet product and (right) mean profiles of shortwave (SW), longwave (LW), and net radiative heating rates for 10 Oct–31 Dec 2011.

which is qualitatively consistent with the moisture anomalies observed during DYNAMO (Fig. 12).

b. Assessment of radiative–convective instability

The possible role of radiative forcing in the dynamics of the MJO can be assessed by comparing column-integrated values of radiative to convective heating. Using a full-physics GCM, Lee et al. (2001) argued that if this ratio exceeds approximately 20%, then the atmosphere can reach radiative–convective instability (Yu et al. 1998; Raymond 2001). However, whether such an instability exists has been proposed to be further dependent on the normalized gross moist stability (NGMS; Neelin and Held 1987; Raymond et al. 2009; Sobel and Maloney 2012). Sobel and Maloney (2013) posit that if the column-integrated radiative to convective heating ratio is greater than NGMS, then an instability can exist. Physically, this means that radiative heating increases the moist static energy in the column faster than the vertical motion and associated circulation can export it.

In Fig. 13, a comparison is shown between the anomalies (based on SOP means, seasonal trends not removed) of column-integrated convective heating

$L_v P_0 + S_0 \equiv \langle Q_{\text{conv}} \rangle$ from the budgets and flux data and $\langle Q_R \rangle$ from the CERES product for DYNAMO (top panel), the ratio of cloud radiative forcing $\langle Q_R \rangle_{\text{CF}}$ to $\langle Q_{\text{conv}} \rangle$ (middle panel), and a time series of TRMM precipitation for the SOP (bottom panel). Past work by Lin and Mapes (2004) using various budget and radiation datasets showed that, for the December 1992 TOGA COARE MJO, the column-integrated radiative heating lagged the column-integrated convective heating by about 5 days and the enhancement to the convective heating was about 10%–15%. This enhancement fell short of the ~20% Lee et al. (2001) estimate as necessary for the atmosphere to reach radiative–convective instability (Yu et al. 1998; Raymond 2001). Lin and Mapes (2004) speculated that the enhancement factor might be larger, exceeding 20%, over the Indian Ocean, and the recent study of Jiang et al. (2011) using satellite and reanalysis data seems to bear this out.

However, Sobel and Maloney (2012, 2013) hypothesize that the existence of radiative–convective instability is dependent not just on the enhancement factor but also its size in relation to NGMS. For DYNAMO, the time series of the column-integrated radiative–convective heating

ratio (middle panel) indicates an enhancement factor mostly between 10% and 20%, exceeding 20% occasionally. These values are comparable to the total NGMS reported by Sobel et al. (2014) using both the DYNAMO budget dataset and ERA-Interim, suggesting from Sobel and Maloney (2013) that radiative–convective instability is indeed a possibility for the DYNAMO MJOs.

8. Vertical flux of moist static energy

The vertical eddy flux of h (or F) provides a measure of the activity of cumulus convection (Yanai et al. 1973). Given the same rainfall rate in two different settings, if F in the midtroposphere is large (small), the precipitation processes producing the rainfall are largely convective (stratiform). The determination of $F(p)$ as a function of time in past field campaigns such as TOGA COARE has been difficult owing to the lack of knowledge about vertical structure of the net radiative heating rate, $Q_R(p)$, as a function of time. As noted earlier, we use the PNNL CombRet Q_R product in the computation of F, but since the cooling is overestimated owing to the lack of high-cloud measurements on Gan Island, we adjust the CombRet $Q_R(p)$ by a constant factor such that its vertical integral matches $\langle Q_R \rangle$ from array-averaged CERES values.[4] In the computation of $F(p)$, we integrate downward from the tropopause assuming the eddy fluxes are zero at that level.

A time series of F for the NSA is shown in Fig. 14. Several levels of deep convective activity are evident. First, in the light-rain periods from 1 to 15 October and 7 to 16 November, the eddy fluxes are confined to the lower troposphere, consistent with the inference from Q_2 in Fig. 5 of shallow, trade-like cumulus at those times. These periods are followed by ~5-day periods of eddy fluxes extending to the midtroposphere (15–20 October and 17–22 November), indicative of cumulus congestus cloud populations (as also inferred from Fig. 5), and then later by ~1-week periods of strong eddy fluxes extending to the upper troposphere. Consistent with the profiles of Q_1 and Q_2 in Fig. 5 and the time series of relative humidity at NSA sites (Fig. 13 of Johnson and Ciesielski 2013), a stepwise evolution of the cloud populations is suggested as opposed to a smooth transition of the cloud fields. However, definitive conclusions on this matter cannot be made from the budgets alone and work is currently underway to relate the budget results to the cloud populations as determined by

---

[4] CombRet data are not available for the period 1–9 Oct, so the vertical profiles for that period are approximated using CombRet $Q(p)$ for the period 12–17 Nov, which had a similar mean relative humidity profile. Both of these periods experienced suppressed conditions and were characterized with similar budget profiles and CERES $\langle Q_R \rangle$.
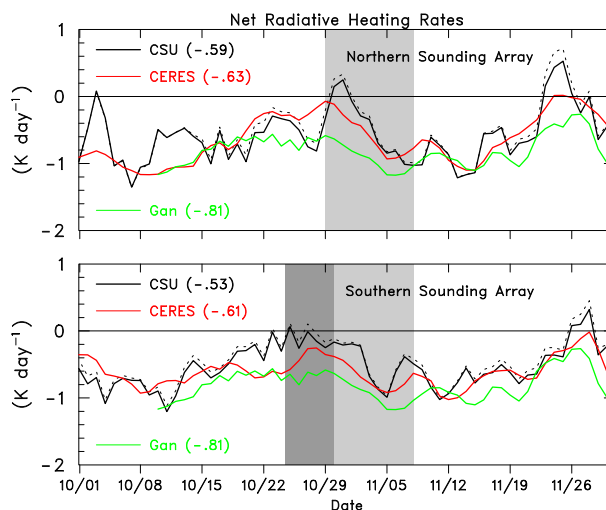

FIG. 11. SOP time series (3-day running-mean filtered, daily average values) of net radiative heating rate (K day^{-1}) from budgets and CERES product for array areas and from PNNL CombRet product for Gan Island, for (top) NSA and (bottom) SSA. Solid (dashed) black curves are $\langle Q_R \rangle$ with (without) inclusion of terms involving the effects of rain (see text). Numbers in parentheses are SOP-mean values. Light (dark) shading denotes periods of R/V *Revelle* (*Mirai*) port calls.

the research radars, similar to the studies of Powell and Houze (2013) and DePasquale et al. (2014). The deeper events in October were associated with westward-moving, 2-day disturbances (Zuluaga and Houze 2013; Johnson and Ciesielski 2013), while those in November were associated with Kelvin waves (Gottschalck et al. 2013; DePasquale et al. 2014). The light-rain periods following the active periods of heaviest rainfall (1–4 and 29–30 November) were characterized by weak eddy fluxes, consistent with a prevalence of stratiform precipitation. These results further support the accumulating evidence of a typical pattern of shallow-to-congestus-to-deep-to-stratiform evolution of precipitation within the MJO but also indicate the shorter transition periods for the November than the October event.

The profiles of F for the SSA are strikingly different (Fig. 15). There are numerous instances of strong eddy fluxes extending to the midtroposphere throughout the 2-month period, consistent with the results shown in Fig. 6. Although there are several strong events timed with the heavy rainfall at the ends of October and November in connection with the MJOs, others occurred in the suppressed phases of the events and are related to episodic disturbances within the ITCZ-like precipitation band south of the equator.

SOP-mean NSA and SSA profiles of $Q_1 - Q_2 - Q_R$ and F, and SSA minus NSA differences in those quantities, are shown in Fig. 16. Once again, the substantially different
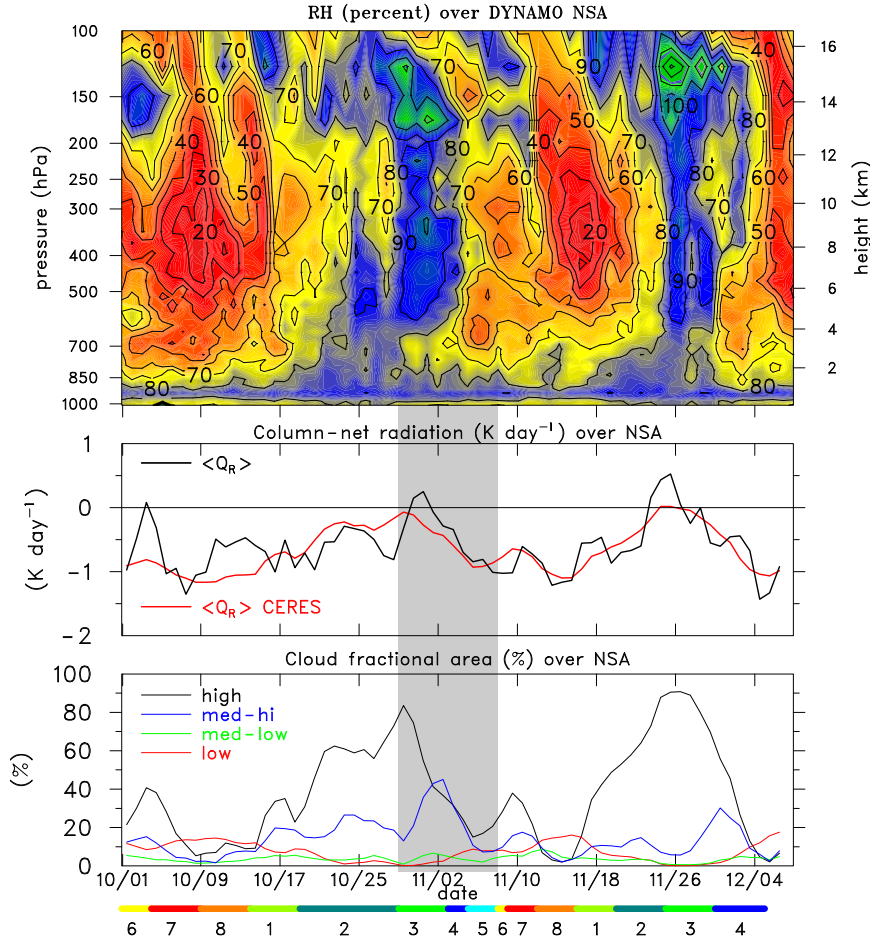
FIG. 12. The 1 Oct–6 Dec time series (3-day running-mean filtered, daily average values) of (top) relative humidity (%, with respect to ice for $T < 0°C$), (middle) $\langle Q_R \rangle$ from budgets (black) and CERES (red), and (bottom) cloud fractional area from CERES for the following definitions of cloud layers: low ($p > 700$ hPa), med-low ($700 > p > 500$ hPa), med-hi ($500 > p > 300$ hPa), and high ($p < 300$ hPa) for NSA. Shaded region denotes period when R/V *Revelle* was off station. RMM index shown below bottom panel.

mean characteristics of convection in the two arrays are evident. The smaller separation of the Q_1 and Q_2 peaks in the NSA leads to smaller values of $Q_1 - Q_2 - Q_R$ (i.e., the eddy flux convergence of moist static energy) in the upper troposphere and weaker eddy fluxes F in the midtroposphere, consistent with the higher stratiform fraction there as supported by the TRMM estimates. Comparison of F_0 from the budgets with $S_0 + L_v E_0$ from TropFlux shown in Fig. 16 indicates good agreement for the NSA (128 vs 115 W m^{-2}, respectively) but slightly poorer agreement for the SSA (138 vs 116 W m^{-2}, respectively).

9. Summary and conclusions

DYNAMO sounding data have been used to determine the apparent heat source Q_1 and apparent

moisture sink Q_2 for the northern and southern sounding arrays (NSA and SSA, respectively) over the central Indian Ocean during the DYNAMO special observing period (SOP; October–November 2011). The sounding data have undergone extensive quality control prior to the computation of the budgets (Ciesielski et al. 2014a). In addition, a procedure has been applied to mitigate the effects of the mountainous island of Sri Lanka on the Colombo soundings (Ciesielski et al. 2014b). Although ECMWF operational analyses have been used to describe the larger-scale characteristics of the flow over the Indian Ocean during DYNAMO, the budget results for the sounding arrays are largely model independent. Surface precipitation rate P_0 from the moisture budget and tropospheric net radiation $\langle Q_R \rangle$ from the combined
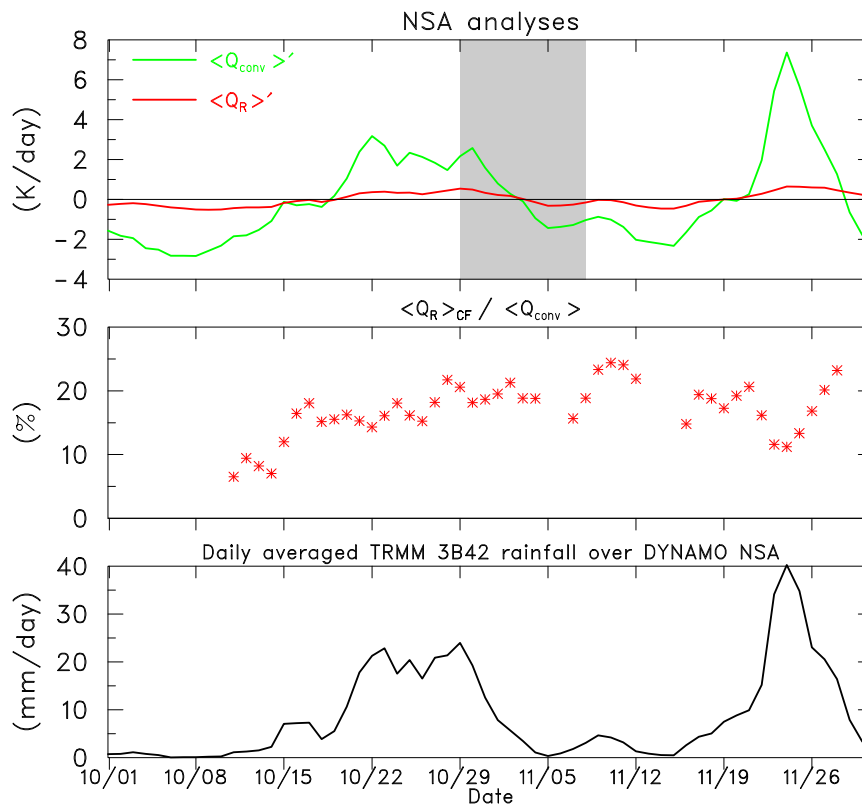
FIG. 13. (top) Comparison of anomalies of CERES $\langle Q_R \rangle$ and convective heating $\langle Q_{\text{conv}} \rangle$ for NSA for DYNAMO SOP based on 3-day running-mean filtered, daily averaged values. (middle) Time series of ratio of cloud radiative forcing $\langle Q_R \rangle_{\text{CF}}$ to $\langle Q_{\text{conv}} \rangle$. Values plotted only when daily TRMM precipitation $> 1\,\text{mm}\,\text{day}^{-1}$. (bottom) TRMM 3B42 rainfall rate (mm day^{-1}) time series for NSA. Shaded region denotes period when R/V *Revelle* was off station.

budgets have been determined by incorporating surface sensible and latent heat flux measurements from TropFlux (Praveen Kumar et al. 2012). The TropFlux measurements show good agreement with the in situ measurements of the bulk fluxes at the R/V *Revelle*. The results for P_0 and $\langle Q_R \rangle$ are compared to independent satellite-based estimates of these quantities. In addition, the availability of vertical profiles of radiative heating rate from the AMIE facility on Gan Island has permitted computations of the vertical profile of the vertical eddy flux of moist static energy. Finally, the budget results and CERES radiation data are used to assess whether radiative–convective instability was operative for the MJOs during DYNAMO.

Principal findings of the study are as follows:

• The spatial and temporal variation of the budget-derived rainfall rate over the Indian Ocean during the SOP shows good agreement with the independent TRMM-based estimates. Moreover, the time series of

array-averaged rainfall rate from the moisture budget agrees well with the satellite-based estimates (TRMM, CMORPH, GPCP, and GSMAP).

• Prominent MJO signals were observed over the NSA, with a sequence of convective system evolution inferred from Q_1 and Q_2 for both the October and November MJOs consistent with numerous previous studies: shallow nonprecipitating cumulus, followed by congestus clouds, then deep convection, and finally stratiform precipitation. The two MJOs were otherwise quite different. Stronger convective moistening by shallow cumulus was observed leading up to the active phase in October than November. The duration of deep convective activity was at least a week longer in the October MJO and consisted of more short duration (2 day) pulses in the heating than in the November MJO, the latter being dominated by two prominent Kelvin wave heating peaks.

• The time series of Q_1 and Q_2 for the SSA were strikingly different from the NSA, characterized by frequent episodes of heating and drying in association with multiple
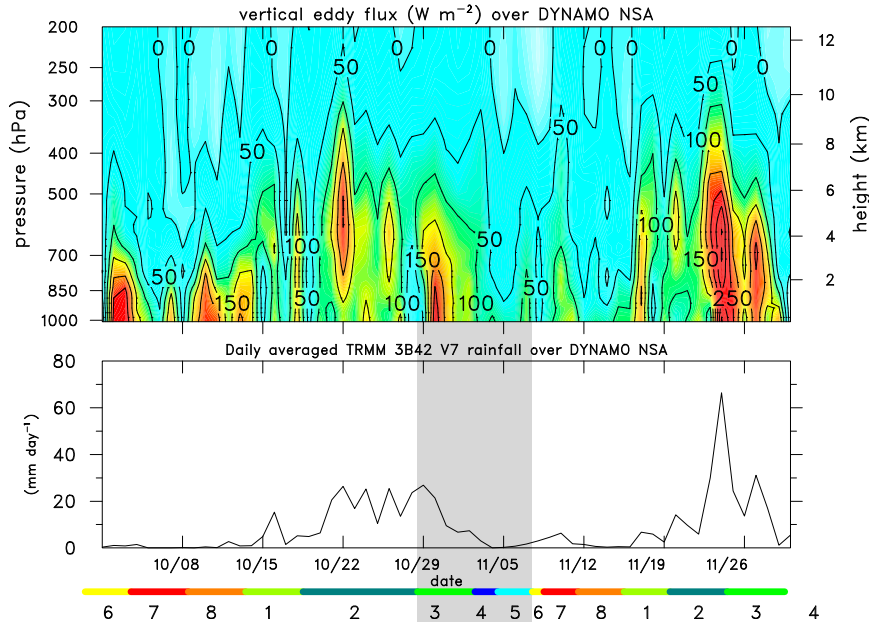
FIG. 14. Time series of daily average values of (top) vertical eddy moist static energy flux F (contour interval: 50 W m^{-2}; shading denotes gradations between intervals) and (bottom) TRMM 3B42v7 rainfall rate (mm day^{-1}) for NSA for DYNAMO SOP. Shaded region denotes period when R/V *Revelle* was off station. RMM index shown below bottom panel.

precipitation events. The MJO signal in the heating was still evident in the SSA but smaller in amplitude and principally manifest at the end of the events.

- The shapes of Q_1 and Q_2 vertical profiles were similar for the NSA but less so for the SSA where the peaks

were widely separated, suggesting a greater stratiform rain fraction over the NSA than the SSA. Though the sampling was limited, TRMM measurements support this finding. The findings also support the work of Lin et al. (2004), which indicates that the
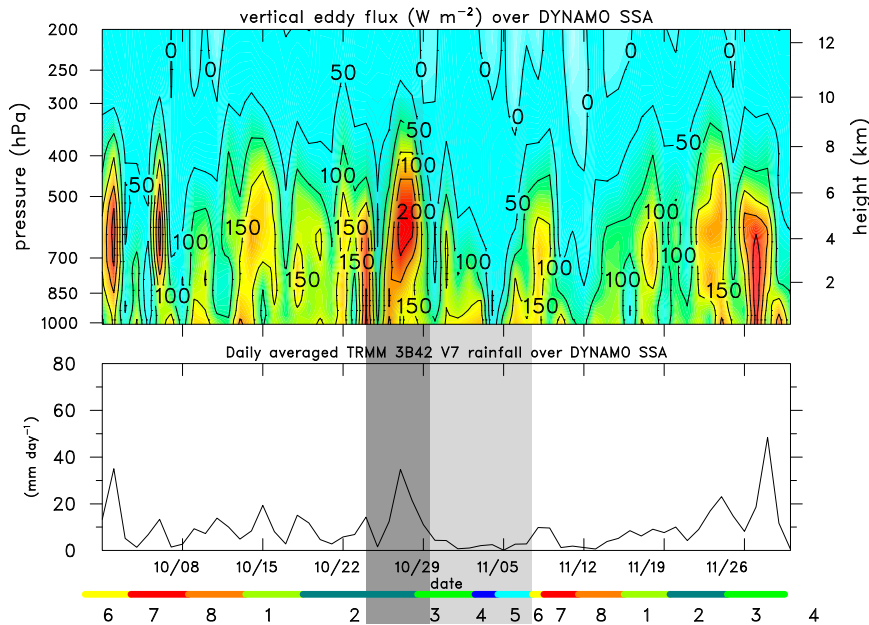

FIG. 15. As in Fig. 14, but for SSA. Dark and light vertical shaded bars indicate times when R/V *Mirai* and *Revelle*, respectively, were off station.
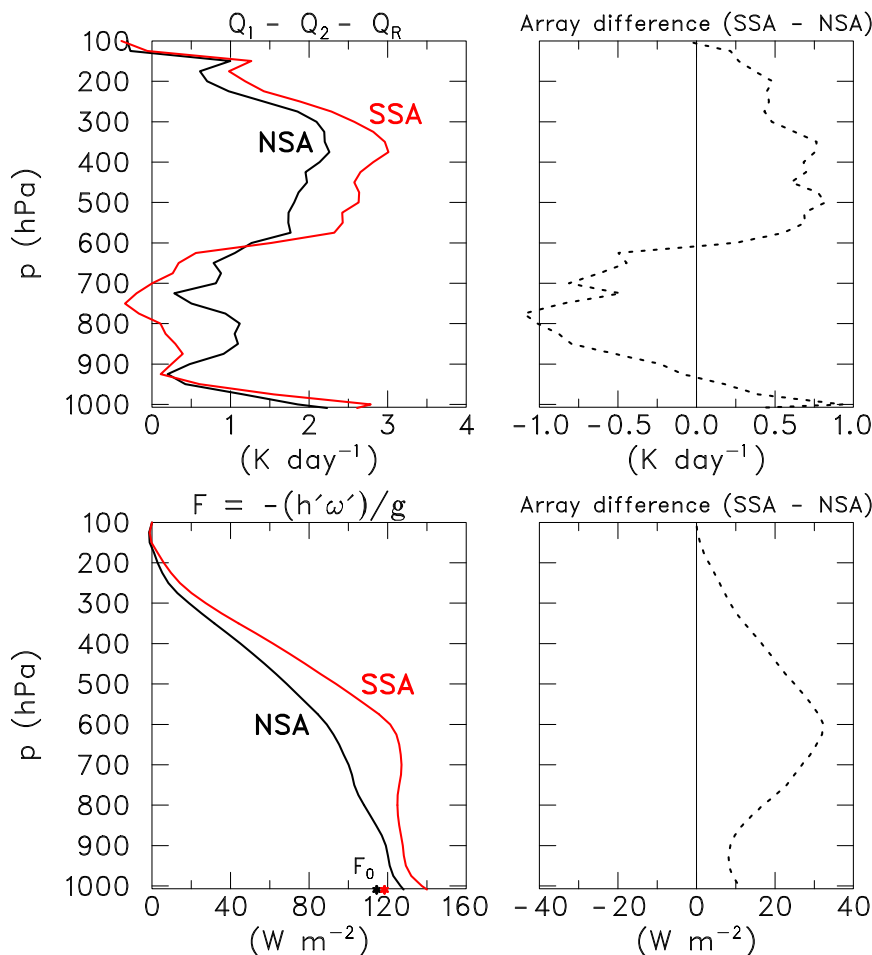
FIG. 16. (top left) SOP-mean profiles of $Q_1 - Q_2 - Q_R$ (K day^{-1}) for NSA and SSA and (top right) SSA minus NSA difference in those quantities. (bottom left) F (W m^{-2}) for NSA and SSA and (bottom right) SSA minus NSA difference in F. Surface sensible plus latent heat flux (F_0) from TropFlux is indicated on the x axis of bottom left panel for NSA (black) and SSA (red).

stratiform rain fraction for the MJO is greater than the tropical mean.

- The time series of $\langle Q_R \rangle$ from the budgets shows reasonable agreement with the satellite-based CERES estimate both indicating a significant modulation of $\langle Q_R \rangle$ by the MJO. High-level clouds during the active phases of the both MJOs reduced the net-column radiative cooling, even reverting $\langle Q_R \rangle$ to weak positive values at times, and indicating the important role of radiation in the moist static energy budget (Sobel et al. 2014). For the NSA, the budget SOP-mean $\langle Q_R \rangle$ was -0.59 K day^{-1} compared to -0.63 K day^{-1} for CERES, while the agreement was slightly poorer for the SSA (-0.53 vs -0.62 K day^{-1}, respectively).

- Vertical profiles of the vertical flux of moist static energy for the NSA support the inferences of the evolving cloud populations in the MJO based on the

Q_1 and Q_2 results alone—namely, a transition from shallow cumulus to congestus to deep convection and finally to stratiform precipitation. There is a suggestion of a stepwise evolution, supportive of past studies (Kikuchi and Takayabu 2004; Yoneyama et al. 2008; Virts and Wallace 2010; Del Genio et al. 2012); however, these findings are regarded as preliminary and require further study. The results for the SSA are again strikingly different, indicating much more frequent episodes of convective activity in the ITCZ, with an absence of the convective evolution seen for the NSA.

- The net tropospheric radiative heating due to the cloud systems was approximately 20%, of the same amplitude as the normalized gross moist stability (Sobel et al. 2014), suggesting a possible role of radiative–convective instability (Yu et al. 1998; Raymond 2001) for the two MJOs.

In addition to the budget analyses presented herein, large-scale forcing fields (e.g., Wu et al. 2000) have been computed and made available for application to cloud-resolving and single-column models. The good agreement between budget integral constraints (i.e., rainfall, $\langle Q_R \rangle$, surface fluxes) lends confidence to the accuracy of the forcing fields and their ability to capture the large-scale signal associated with the MJO. The forcing datasets used in this study are available from the National Center for Atmospheric Research Earth Observation Laboratory DYNAMO archive (http://data.eol.ucar.edu/master_list/?project=DYNAMO).

Although the above results have yielded insight into the convective heating profiles and inferences regarding cloud populations in the DYNAMO MJOs, further work is needed to directly relate these findings to the research radar observations of precipitation systems at the S-PolKa site on Gan Island, the TOGA radar on the R/V *Revelle*, and the 5-cm radar on the R/V *Mirai*, as well as cloud radar observations on Gan Island. This work is currently underway. In addition, we have not explored in this study the diurnal cycle of convection, which turns out to be particularly important during the suppressed phases of the MJOs (see Ruppert and Johnson 2015).

REFERENCES

Adler, R. F., and Coauthors, 2003: The Version-2 Global Precipitation Climatology Project (GPCP) monthly precipitation analysis (1979–present). *J. Hydrometeor.,* **4,** 1147–1167, doi:10.1175/1525-7541(2003)004<1147:TVGPCP>2.0.CO;2.

Ao, C. O., T. K. Meehan, G. A. Hajj, A. J. Mannucci, and G. Beyerle, 2003: Lower-tropospheric refractivity bias in GPS occultation retrievals. *J. Geophys. Res.,* **108,** 4577, doi:10.1029/2002JD003216.

Aonashi, K., and Coauthors, 2009: GSMaP passive, microwave precipitation retrieval algorithm: Algorithm description and validation. *J. Meteor. Soc. Japan,* **87A,** 119–136, doi:10.2151/jmsj.87A.119.

Barnes, H. C., and R. A. Houze Jr., 2013: The precipitating cloud population of the Madden-Julian Oscillation over the Indian and west Pacific Ocean. *J. Geophys. Res. Atmos.,* **118,** 6996–7023, doi:10.1002/jgrd.50375.

Benedict, J., and D. A. Randall, 2007: Observed characteristics of the MJO relative to maximum rainfall. *J. Atmos. Sci.,* **64,** 2332–2354, doi:10.1175/JAS3968.1.

Chikira, M., 2014: Easward-propagating instraseasonal oscillation represented by Chikira–Sugiyama cumulus parameterization. Part II: Understanding moisture variation under weak temperature gradient balance. *J. Atmos. Sci.,* **71,** 615–639, doi:10.1175/JAS-D-13-038.1.

Ciesielski, P. E., L. Hartten, and R. H. Johnson, 1997: Impacts of merging profiler and rawinsonde winds on TOGA COARE analyses. *J. Atmos. Oceanic Technol.,* **14,** 1264–1279, doi:10.1175/1520-0426(1997)014<1264:IOMPAR>2.0.CO;2.

——, R. H. Johnson, P. T. Haertel, and J. Wang, 2003: Corrected TOGA COARE sounding humidity data: Impact on diagnosed properties of convection and climate over the warm pool. *J. Climate,* **16,** 2370–2384, doi:10.1175/2790.1.

——, and Coauthors, 2014a: Quality controlled upper-air sounding dataset for DYNAMO/CINDY/AMIE: Development and corrections. *J. Atmos. Oceanic Technol.,* **31,** 741–764, doi:10.1175/JTECH-D-13-00165.1.

——, R. H. Johnson, K. Yoneyama, and R. K. Taft, 2014b: Mitigation of Sri Lanka island effects in Colombo sounding data its impact on DYNAMO analyses. *J. Meteor. Soc. Japan,* **92,** 385–405, doi:10.2151/jmsj.2014-407.

Del Genio, A. D., Y. Chen, D. Kim, and M.-S. Yao, 2012: The MJO transition from shallow to deep convection in *CloudSat/CALIPSO* and GISS GCM simulations. *J. Climate,* **25,** 3755–3770, doi:10.1175/JCLI-D-11-00384.1.

DePasquale, A., C. Schumacher, and A. Rapp, 2014: Radar observations of MJO and Kelvin wave interactions during DYNAMO/CINDY2011/AMIE. *J. Geophys. Res. Atmos.,* **119,** 6347–6367, doi:10.1002/2013JD021031.

Emanuel, K. A., and M. Bister, 1996: Moist convective velocity and buoyancy scales. *J. Atmos. Sci.,* **53,** 3276–3285, doi:10.1175/1520-0469(1996)053<3276:MCVABS>2.0.CO;2.

Fairall, C. W., E. F. Bradley, D. P. Rogers, J. B. Edson, and G. S. Young, 1996: Bulk parameterization of air-sea fluxes for TOGA COARE. *J. Geophys. Res.,* **101,** 3747–3764, doi:10.1029/95JC03205.

Feng, Z., S. A. McFarlane, C. Schumacher, S. Ellis, and N. Bharadwaj, 2014: Constructing a merged cloud–precipitation radar dataset for tropical clouds during the DYNAMO/AMIE experiment on Addu Atoll. *J. Atmos. Oceanic Technol.,* **31,** 1021–1042, doi:10.1175/JTECH-D-13-00132.1.

Figa-Saldaña, J., J. J. W. Wilson, E. Attema, R. Gelsthorpe, M. R. Drinkwater, and A. Stoffelen, 2002: The advanced scatterometer (ASCAT) on the meteorological operational (MetOp) platform: A follow on for European wind scatterometers. *Can. J. Remote Sens.,* **28,** 404–412, doi:10.5589/m02-035.

Funk, A., C. Schumacher, and J. Awaka, 2013: Analysis of rain classifications over the tropics by version 7 of the TRMM PR 2A23 algorithm. *J. Meteor. Soc. Japan,* **91,** 257–272, doi:10.2151/jmsj.2013-302.

Gosnell, R., C. W. Fairall, and P. J. Webster, 1995: The sensible heat of rainfall in the tropical ocean. *J. Geophys. Res.,* **100,** 18 437–18 442, doi:10.1029/95JC01833.

Gottschalck, J., P. E. Roundy, C. J. Schreck III, A. Vintzileos, and C. Zhang, 2013: Large-scale atmospheric and oceanic conditions during the 2011–12 DYNAMO field campaign. *Mon. Wea. Rev.,* **141,** 4173–4196, doi:10.1175/MWR-D-13-00022.1.

Haertel, P. T., G. N. Kiladis, A. Denno, and T. M. Rickenbach, 2008: Vertical-mode decompositions of 2-day waves and the Madden–Julian oscillation. *J. Atmos. Sci.,* **65,** 813–833, doi:10.1175/2007JAS2314.1.

Hartmann, D. L., H. H. Hendon, and R. A. Houze Jr., 1984: Some implications of the mesoscale circulations in tropical cloud clusters for large-scale dynamics and climate. *J. Atmos. Sci.,* **41,** 113–121, doi:10.1175/1520-0469(1984)041<0113:SIOTMC>2.0.CO;2.

——, M. E. Ockert-Bell, and M. L. Michelsen, 1992: The effect of cloud type on the Earth's energy balance: Global analysis. *J. Climate,* **5,** 1281–1304, doi:10.1175/1520-0442(1992)005<1281:TEOCTO>2.0.CO;2.

Hohenegger, C., and B. Stevens, 2013: Preconditioning deep convection with cumulus congestus. *J. Atmos. Sci.,* **70,** 448–464, doi:10.1175/JAS-D-12-089.1.

Holmlund, K., C. S. Velden, and M. Rohn, 2001: Enhanced automated quality control applied to high-density satellite-derived winds. *Mon. Wea. Rev.,* **129,** 517–529, doi:10.1175/1520-0493(2001)129<0517:EAQCAT>2.0.CO;2.

Huffman, G. J., R. F. Adler, D. T. Bolvin, G. Gu, E. J. Nelkin, K. P. Bowman, E. F. Stocker, and D. B. Wolff, 2007: The TRMM Multisatellite Precipitation Analysis: Quasi-global, multiyear, combined-sensor precipitation estimates at fine scale. *J. Hydrometeor.,* **8,** 38–55, doi:10.1175/JHM560.1.

Hung, M.-P., J.-L. Lin, W. Wang, D. Kim, T. Shinoda, and S. J. Weaver, 2013: MJO and convectively coupled equatorial waves simulated by CMIP5 climate models. *J. Climate,* **26,** 6185–6214, doi:10.1175/JCLI-D-12-00541.1.

Jiang, X., and Coauthors, 2011: Vertical diabatic heating structure of the MJO: Intercomparison between recent reanalyses and TRMM. *Mon. Wea. Rev.,* **139,** 3208–3223, doi:10.1175/2011MWR3636.1.

Johnson, R. H., 1980: Diagnosis of convective and meso-scale motions during Phase III of GATE. *J. Atmos. Sci.,* **37,** 733–753, doi:10.1175/1520-0469(1980)037<0733:DOCAMM>2.0.CO;2.

——, and X. Lin, 1997: Episodic trade wind regimes over the western Pacific warm pool. *J. Atmos. Sci.,* **54,** 2020–2034, doi:10.1175/1520-0469(1997054<2020:ETWROT>2.0.CO);2.

——, and P. E. Ciesielski, 2000: Rainfall and radiative heating rate estimates from TOGA COARE atmospheric budgets. *J. Atmos. Sci.,* **57,** 1497–1514, doi:10.1175/1520-0469(2000)057<1497:RARHRF>2.0.CO;2.

——, and ——, 2002: Characteristics of the 1998 summer monsoon onset over the northern South China Sea. *J. Meteor. Soc. Japan,* **80,** 561–578, doi:10.2151/jmsj.80.561.

——, and ——, 2013: Structure and properties of Madden–Julian oscillations deduced from DYNAMO sounding arrays. *J. Atmos. Sci.,* **70,** 3157–3179, doi:10.1175/JAS-D-13-065.1.

——, T. M. Rickenbach, S. A. Rutledge, P. E. Ciesielski, and W. H. Schubert, 1999: Trimodal characteristics of tropical convection. *J. Climate,* **12,** 2397–2418, doi:10.1175/1520-0442(1999)012<2397:TCOTC>2.0.CO;2.

Joyce, R. J., J. E. Janowiak, P. A. Arkin, and P. Xie, 2004: A method that produces global precipitation estimates from passive microwave and infrared data at high spatial and temporal resolution. *J. Hydrometeor.,* **5,** 487–503, doi:10.1175/1525-7541(2004)005<0487:CAMTPG>2.0.CO;2.

Katsumata, M., P. E. Ciesielski, and R. H. Johnson, 2011: Evaluation of budget analysis during MISMO. *J. Appl. Meteor. Climatol.,* **50,** 241–254, doi:10.1175/2010JAMC2515.1.

Kikuchi, K., and Y. N. Takayabu, 2004: The development of organized convection associated with the MJO during TOGA COARE IOP: Trimodal characteristics. *Geophys. Res. Lett.,* **31,** L10101, doi:10.1029/2004GL019601.

Kiladis, G. N., K. H. Straub, G. C. Reid, and K. S. Gage, 2001: Aspects of interannual and intraseasonal variability of the tropopause and lower stratosphere. *Quart. J. Roy. Meteor. Soc.,* **127,** 1961–1983, doi:10.1002/qj.49712757606.

——, ——, and P. T. Haertel, 2005: Zonal and vertical structure of the Madden–Julian oscillation. *J. Atmos. Sci.,* **62,** 2790–2809, doi:10.1175/JAS3520.1.

——, M. C. Wheeler, P. T. Haertel, K. H. Straub, and P. E. Roundy, 2009: Convectively coupled equatorial waves. *Rev. Geophys.,* **47,** 2003, doi:10.1029/2008RG000266.

Kubota, T., and Coauthors, 2007: Global precipitation map using satellite-borne microwave radiometers by the GSMaP Project: Production and validation. *IEEE Trans. Geosci. Remote Sens.,* **45,** 2259–2275, doi:10.1109/TGRS.2007.895337.

Kuo, Y.-H., T.-K. Lee, S. Sokolovskiy, C. Rocken, W. Schreiner, D. Hunt, and R. A. Anthes, 2004: Inversion and error estimation of GPS radio occultation data. *J. Meteor. Soc. Japan,* **82,** 507–531, doi:10.2151/jmsj.2004.507.

L'Ecuyer, T. S., and G. McGarragh, 2010: A 10-year climatology of tropical radiative heating and its vertical structure from TRMM observations. *J. Climate,* **23,** 519–541, doi:10.1175/2009JCLI3018.1.

Lee, M.-I., I.-S. Kang, J.-K. Kim, and B. E. Mapes, 2001: Influence of cloud-radiation interaction on simulating tropical intraseasonal oscillation with an atmosphere general circulation model. *J. Geophys. Res.,* **106,** 14 291–14 233, doi:10.1029/2001JD900143.

Lin, J.-L., and B. E. Mapes, 2004: Radiation budget of the tropical intraseasonal oscillation. *J. Atmos. Sci.,* **61,** 2050–2062, doi:10.1175/1520-0469(2004)061<2050:RBOTTI>2.0.CO;2.

——, ——, M. Zhang, and N. Newman, 2004: Stratiform precipitation, vertical heating profiles, and the Madden–Julian oscillation. *J. Atmos. Sci.,* **61,** 296–309, doi:10.1175/1520-0469(2004)061<0296:SPVHPA>2.0.CO;2.

Lin, X., and R. H. Johnson, 1996: Heating, moistening, and rainfall over the western Pacific warm pool during TOGA COARE. *J. Atmos. Sci.,* **53,** 3367–3383, doi:10.1175/1520-0469(1996)053<3367:HMAROT>2.0.CO;2.

Liu, C., E. J. Zipser, and S. W. Nesbitt, 2007: Global distribution of tropical deep convection: Different perspectives from TRMM infrared and radar data. *J. Climate,* **20,** 489–503, doi:10.1175/JCLI4023.1.

Luo, H., and M. Yanai, 1984: The large-scale circulation and heat sources over the Tibetan Plateau and surrounding areas during the early summer of 1979. Part II: Heat and moisture budgets. *Mon. Wea. Rev.,* **112,** 966–989, doi:10.1175/1520-0493(1984)112<0966:TLSCAH>2.0.CO;2.

Madden, R. A., and P. R. Julian, 1972: Description of global-scale circulation cells in the tropics with a 40–50 day period. *J. Atmos. Sci.,* **29,** 1109–1123, doi:10.1175/1520-0469(1972)029<1109:DOGSCC>2.0.CO;2.

Mapes, B. E., P. E. Ciesieslki, and R. H. Johnson, 2003: Sampling errors in rawinsonde-array budgets. *J. Atmos. Sci.,* **60,** 2697–2714, doi:10.1175/1520-0469(2003)060<2697:SEIRB>2.0.CO;2.

——, S. Tulich, J. Lin, and P. Zuidema, 2006: The mesocale convection life cycle: Building block or prototype for large-scale tropical waves? *Dyn. Atmos. Oceans,* **42,** 3–29, doi:10.1016/j.dynatmoce.2006.03.003.

McNab, A. L., and A. K. Betts, 1978: Mesoscale budget study of cumulus convection. *Mon. Wea. Rev.,* **106,** 1317–1331, doi:10.1175/1520-0493(1978)106<1317:AMBSOC>2.0.CO;2.

Neelin, J. D., and I. M. Held, 1987: Modeling tropical convergence based on the moist static energy budget. *Mon. Wea. Rev.,* **115,** 3–12, doi:10.1175/1520-0493(1987)115<0003:MTCBOT>2.0.CO;2.

Ooyama, K., 1990: A thermodynamic foundation for modeling the moist atmosphere. *J. Atmos. Sci.,* **47,** 2580–2593, doi:10.1175/1520-0469(1990)047<2580:ATFFMT>2.0.CO;2.

Powell, S. W., and R. A. Houze Jr., 2013: The cloud population and the onset of the Madden-Julian Oscillation over the Indian Ocean during DYNAMO-AMIE. *J. Geophys. Res. Atmos.,* **118,** 11 979–11 995, doi:10.1002/2013JD020421.

Praveen Kumar, B., J. Vialard, M. Lengaigne, V. S. N. Murty, and M. J. McPhaden, 2012: TropFlux: Air-sea fluxes for the global tropical oceans—Description and evaluation. *Climate Dyn.,* **38,** 1521–1543, doi:10.1007/s00382-011-1115-0.

Randall, D. A., Harshvardhan, D. A. Dazlich, and T. G. Corsetti, 1989: Interactions among radiation, convection, and large-scale dynamics in a general circulation model. *J. Atmos. Sci.,* **46,** 1943–1970, doi:10.1175/1520-0469(1989)046<1943:IARCAL>2.0.CO;2.

Raymond, D. J., 2000: The Hadley circulation as a radiative-convective instability. *J. Atmos. Sci.,* **57,** 1286–1297, doi:10.1175/1520-0469(2000)057<1286:THCAAR>2.0.CO;2.

——, 2001: A new model of the Madden–Julian oscillation. *J. Atmos. Sci.,* **58,** 2807–2819, doi:10.1175/1520-0469(2001)058<2807:ANMOTM>2.0.CO;2.

——, S. L. Sessions, A. H. Sobel, and Ž. Fuchs, 2009: The mechanics of gross moist stability. *J. Adv. Model. Earth Syst.,* **1,** 9, doi:10.3894/JAMES.2009.1.9.

Ruppert, J. H., and R. H. Johnson, 2015: Diurnally modulated cumulus moistening in the preonset stage of the Madden–Julian oscillation during DYNAMO. *J. Atmos. Sci.,* doi:10.1175/JAS-D-14-0218.1, in press.

Schumacher, C., and R. A. Houze Jr., 2003: Stratiform rain in the tropics as seen by the TRMM Precipitation Radar. *J. Climate,* **16,** 1739–1756, doi:10.1175/1520-0442(2003)016<1739:SRITTA>2.0.CO;2.

Sherwood, S. C., V. Ramanathan, T. P. Barnett, M. K. Tyree, and E. Roeckner, 1994: Response of an atmospheric general circulation model to radiative forcing of tropical clouds. *J. Geophys. Res.,* **99,** 20 829–20 845, doi:10.1029/94JD01632.

Slingo, A., and J. M. Slingo, 1988: The response of a general circulation model to cloud longwave radiative forcing. I: Introduction and initial experiments. *Quart. J. Roy. Meteor. Soc.,* **114,** 1027–1062, doi:10.1002/qj.49711448209.

——, and ——, 1991: The response of a general circulation model to cloud longwave radiative forcing. II: Further studies. *Quart. J. Roy. Meteor. Soc.,* **117,** 333–364, doi:10.1002/qj.49711749805.

Sobel, A., and E. D. Maloney, 2012: An idealized semi-empirical framework for the Madden–Julian oscillation. *J. Atmos. Sci.,* **69,** 1691–1705, doi:10.1175/JAS-D-11-0118.1.

——, and ——, 2013: Moisture modes and the eastward propagation of the MJO. *J. Atmos. Sci.,* **70,** 187–192, doi:10.1175/JAS-D-12-0189.1.

——, S. Wang, and D. Kim, 2014: Moist static energy budget of the MJO during DYNAMO. *J. Atmos. Sci.,* **71,** 4276–4291, doi:10.1175/JAS-D-14-0052.1.

Stephens, G. L., M. J. Webb, P. J. Minnett, P. H. Daum, L. Kleinman, I. Wittmeyer, and D. A. Randall, 1994: Observations of the Earth's radiation budget in relation to atmospheric

hydrology. 4: Atmospheric column radiative cooling over the world's oceans. *J. Geophys. Res.,* **99,** 18 585–18 604, doi:10.1029/94JD01151.

——, P. J. Webster, R. H. Johnson, R. Engelen, and T. S. L'Ecuyer, 2004: Observational evidence for the mutual regulation of the tropical hydrological cycle and the tropical sea surface temperatures. *J. Climate,* **17,** 2213–2224, doi:10.1175/1520-0442(2004)017<2213:OEFTMR>2.0.CO;2.

Tao, W.-K., C.-L. Shie, D. Johnson, S. Braun, R. H. Johnson, and P. E. Ciesielski, 2003: Convective systems over the South China Sea: Cloud-resolving model simulations. *J. Atmos. Sci.,* **60,** 2929–2956, doi:10.1175/1520-0469(2003)060<2929:CSOTSC>2.0.CO;2.

Thuburn, J., and G. C. Craig, 2002: On the temperature structure of the tropical substratosphere. *J. Geophys. Res.,* **107,** doi:10.1029/2001JD000448.

Trenberth, K. E., 1991: Climate diagnostics from global analyses: Conservation of mass in ECMWF analyses. *J. Climate,* **4,** 707–722, doi:10.1175/1520-0442(1991)004<0707:CDFGAC>2.0.CO;2.

Tung, W.-W., C. Lin, B. Chen, M. Yanai, and A. Arakawa, 1999: Basic modes of cumulus heating and drying observed during TOGA-COARE IOP. *Geophys. Res. Lett.,* **26,** 3117–3120, doi:10.1029/1999GL900607.

Virts, K. S., and J. M. Wallace, 2010: Annual, interannual, and intraseasonal variability of tropical tropopause transition layer cirrus. *J. Atmos. Sci.,* **67,** 3113–3129, doi:10.1175/2010JAS3412.1.

——, ——, Q. Fu, and T. P. Ackerman, 2010: Tropical tropopause transition layer cirrus as represented by CALIPSO lidar observations. *J. Atmos. Sci.,* **67,** 3113–3129, doi:10.1175/2010JAS3412.1.

Waite, M. L., and B. Khouider, 2010: The deepening of tropical convection by congestus preconditioning. *J. Atmos. Sci.,* **67,** 2601–2615, doi:10.1175/2010JAS3357.1.

Wang, J., H. L. Cole, D. J. Carlson, E. R. Miller, K. Beierle, A. Paukkunen, and T. K. Laine, 2002: Corrections of the humidity measurement errors from the Vaisala RS80 radiosonde—Application to TOGA COARE data. *J. Atmos. Oceanic Technol.,* **19,** 981–1002, doi:10.1175/1520-0426(2002)019<0981:COHMEF>2.0.CO;2.

Webster, P. J., 1994: TOGA COARE: The role of hydrological processes in ocean-atmosphere interaction. *Rev. Geophys.,* **32,** 427–476, doi:10.1029/94RG01873.

——, and R. Lukas, 1992: TOGA COARE: The Coupled Ocean–Atmosphere Response Experiment. *Bull. Amer. Meteor. Soc.,* **73,** 1377–1416, doi:10.1175/1520-0477(1992)073<1377:TCTCOR>2.0.CO;2.

Weller, R. A., and S. P. Anderson, 1996: Surface meteorology and air–sea fluxes in the western equatorial Pacific warm pool during the TOGA Coupled Ocean–Atmosphere Response Experiment. *J. Climate,* **9,** 1959–1990, doi:10.1175/1520-0442(1996)009<1959:SMAASF>2.0.CO;2.

Wheeler, M. C., and H. H. Hendon, 2004: An all-season real-time multivariate MJO index: Development of an index for monitoring and prediction. *Mon. Wea. Rev.,* **132,** 1917–1932, doi:10.1175/1520-0493(2004)132<1917:AARMMI>2.0.CO;2.

Wielicki, B. A., B. R. Barkstrom, E. F. Harrison, R. B. Lee III, G. L. Smith, and J. E. Cooper, 1996: Clouds and the Earth's Radiant Energy System (CERES): An Earth Observing System experiment. *Bull. Amer. Meteor. Soc.,* **77,** 853–868, doi:10.1175/1520-0477(1996)077<0853:CATERE>2.0.CO;2.

Wu, X., M. W. Moncrieff, and K. A. Emanuel, 2000: Evaluation of large-scale forcing during TOGA COARE for

cloud-resolving models and single-column models. *J. Atmos. Sci.,* **57,** 2977–2985, doi:10.1175/1520-0469(2000)057<2977:EOLSFD>2.0.CO;2.

Xu, W., and S. A. Rutledge, 2014: Convective characteristics of the Madden–Julian oscillation over the central Indian Ocean observed by shipborne radar during DYNAMO. *J. Atmos. Sci.,* **71,** 2859–2877, doi:10.1175/JAS-D-13-0372.1.

Yanai, M., and R. H. Johnson, 1993: Impacts of cumulus convection on thermodynamic fields. *The Representation of Cumulus Convection in Numerical Models, Meteor. Monogr.,* No. 46, Amer. Meteor. Soc., 39–62.

——, S. Esbensen, and J.-H. Chu, 1973: Determination of bulk properties of tropical cloud clusters from large-scale heat and moisture budgets. *J. Atmos. Sci.,* **30,** 611–627, doi:10.1175/1520-0469(1973)030<0611:DOBPOT>2.0.CO;2.

Yoneyama, K., and Coauthors, 2008: MISMO field experiment in the equatorial Indian Ocean. *Bull. Amer. Meteor. Soc.,* **89,** 1889–1903, doi:10.1175/2008BAMS2519.1.

——, C. Zhang, and C. N. Long, 2013: Tracking pulses of the Madden–Julian oscillation. *Bull. Amer. Meteor. Soc.,* **94,** 1871–1891, doi:10.1175/BAMS-D-12-00157.1.

Yu, J.-Y., C. Chou, and J. D. Neelin, 1998: Estimating the gross moist stability of the tropical atmosphere. *J. Atmos. Sci.,* **55,** 1354–1372, doi:10.1175/1520-0469(1998)055<1354:ETGMSO>2.0.CO;2.

Yu, L., and R. A. Weller, 2007: Objectively analyzed air–sea heat fluxes for the global ice-free oceans (1981–2005). *Bull. Amer. Meteor. Soc.,* **88,** 527–539, doi:10.1175/BAMS-88-4-527.

Yuan, J., and R. A. Houze Jr., 2013: Deep convective systems observed by A-Train in the tropical Indo-Pacific region affected by the MJO. *J. Atmos. Sci.,* **70,** 465–486, doi:10.1175/JAS-D-12-057.1.

Zhang, C., 2005: Madden-Julian Oscillation. *Rev. Geophys.,* **43,** RG2003, doi:10.1029/2004RG000158.

——, 2013: The Madden–Julian oscillation: Bridging weather and climate. *Bull. Amer. Meteor. Soc.,* **94,** 1849–1870, doi:10.1175/BAMS-D-12-00026.1.

——, J. Gottschalck, E. D. Maloney, M. W. Moncrieff, F. Vitart, D. E. Waliser, B. Wang, and M. C. Wheeler, 2013: Cracking the MJO nut. *Geophys. Res. Lett.,* **40,** 1223–1230, doi:10.1002/grl.50244.

Zuluaga, M. D., and R. A. Houze Jr., 2013: Evolution of the population of precipitating convective systems over the equatorial Indian Ocean in active phases of the Madden–Julian oscillation. *J. Atmos. Sci.,* **70,** 2713–2725, doi:10.1175/JAS-D-12-0311.1.